



HAL
open science

Glacier, permafrost and thermokarst interactions in Alpine terrain: Insights from seven decades of reconstructed dynamics of the Chauvet glacial and periglacial system (Southern French Alps)

Diego Cusicanqui, Xavier Bodin, Pierre-allain Duvillard, Philippe Schoeneich, André Revil, Alain Assier, Johan Berthet, Michel Peyron, Stéphane Roudnitska, Antoine Rabatel

► To cite this version:

Diego Cusicanqui, Xavier Bodin, Pierre-allain Duvillard, Philippe Schoeneich, André Revil, et al.. Glacier, permafrost and thermokarst interactions in Alpine terrain: Insights from seven decades of reconstructed dynamics of the Chauvet glacial and periglacial system (Southern French Alps). *Earth Surface Processes and Landforms*, 2023, 48 (13), pp.2595-2612. 10.1002/esp.5650 . hal-04262024v2

HAL Id: hal-04262024


<https://hal.science/hal-04262024v2>

Submitted on 27 Oct 2023

HAL is a multi-disciplinary open access archive for the deposit and dissemination of scientific research documents, whether they are published or not. The documents may come from teaching and research institutions in France or abroad, or from public or private research centers.

L'archive ouverte pluridisciplinaire **HAL**, est destinée au dépôt et à la diffusion de documents scientifiques de niveau recherche, publiés ou non, émanant des établissements d'enseignement et de recherche français ou étrangers, des laboratoires publics ou privés.

Glacier, permafrost and thermokarst interactions in Alpine terrain: Insights from seven decades of reconstructed dynamics of the Chauvet glacial and periglacial system (Southern French Alps)

Diego Cusicanqui^{1,2}  | Xavier Bodin² | Pierre-Allain Duvillard^{2,3} | Philippe Schoeneich⁴ | André Revil² | Alain Assier⁴ | Johan Berthet^{2,3} | Michel Peyron⁵ | Stéphane Roudnitska⁵ | Antoine Rabatel¹

¹Université Grenoble Alpes, CNRS, IRD, Grenoble-INP, Institut de Géosciences de l'Environnement (IGE), Grenoble, France

²Université Savoie Mont-Blanc, CNRS, Laboratoire EDYTEM, Le Bourget du Lac, France

³STYX 4D, Le Bourget du Lac, France

⁴Université Grenoble Alpes, Institut d'Urbanisme et Géographie Alpine (IUGA-Pacte), Grenoble, France

⁵Service Restauration Terrain Montagne (RTM), Gap, France

Correspondence

Diego Cusicanqui, Université Grenoble Alpes, CNRS, IRD, Grenoble-INP, Institut de Géosciences de l'Environnement, Grenoble F-38000, France.
Email: diego.cusicanqui@univ-grenoble-alpes.fr

Xavier Bodin, Université Savoie Mont-Blanc, CNRS, Laboratoire EDYTEM, Le Bourget du Lac, France.
Email: xavier.bodin@univ-smb.fr

Funding information

French National Research Agency, Grant/Award Numbers: ANR-15-IDEX-02, ANR10 LABX56; European Regional Development Fund, Grant/Award Number: POIA PA0004100

Abstract

This study analyses the long-term dynamics in the Chauvet glacial and periglacial system (southern French Alps) over seven decades (1948–2020), where several lake outburst floods have been documented since 1930. To accurately describe and explain the complex dynamics of this site, our multidisciplinary approach combines (1) photogrammetry of historical aerial photographs and modern high-resolution satellite and UAV images, (2) geophysical surveys and (3) geomorphological mapping. We provide evidence for spatial and functional interactions between glacial and periglacial features, especially in the lower sector where different landforms with variable ice- and debris-content and specific dynamics are interplayed. We found the highest thinning rates on ice-rich terrain located in the central part of the valley bottom, which, together with bedrock morphology, most probably determine the location of the thermokarst. We also documented an overall acceleration of the creeping of the landforms after the 2000s, with a flow direction largely oriented towards the thermokarst depression. The outburst water flowed through a conduit whose successive opening and closure seem to mainly depend on the rate of lateral convergence of left- and right-hand landforms and on the rate of ice melting (and roof collapse) along the conduit walls. Today, the site of Chauvet still represents a potential hazard for the region due to the large water storage capacity (up to $180\,000 \pm 450\text{ m}^3$) and the development of a predominantly bucket shape in the thermokarst sector.

KEYWORDS

electrical resistivity, French Alps, glacier-permafrost, GLOFs, mountain permafrost, photogrammetry, rock glaciers, thermokarst lakes

1 | INTRODUCTION

Mountain environments are among the most sensitive to climate change, especially the main elements of the cryosphere that are glaciers, permafrost and snow (Hock et al., 2019). On the one hand, the rapid warming during the last decades has accelerated glacier down-wasting rates (Hugonnet et al., 2021). On the other hand, evidences

of degradation of mountain permafrost are widespread, with geomorphological phenomena such as increasing rockfalls (Raveland & Deline, 2015) and accelerating creep of rock glacier permafrost (Marcer et al., 2021), both largely related to the increase in ground temperatures (Etzelmüller et al., 2020).

In high mountains areas, glaciers and permafrost can interact in several ways in various spatial and temporal dimensions

This is an open access article under the terms of the [Creative Commons Attribution](https://creativecommons.org/licenses/by/4.0/) License, which permits use, distribution and reproduction in any medium, provided the original work is properly cited.

© 2023 The Authors. *Earth Surface Processes and Landforms* published by John Wiley & Sons Ltd.

(e.g., Haeberli, 2005). For instance, as observed by Bosson & Lambiel (2016) on small high altitude valleys in the French and Swiss Alps, where complex assemblages of glaciers, debris-covered glaciers and rock glaciers (hereafter called glacial and periglacial systems) were observed. The dynamics of each component is related to very specific surface lowering and downslope movement. The responses of these spatially connected components to climate forcing can be partly attributed to the variable thickness of the superficial debris layer, which controls the energy balance and hence the thermal regime of permafrost and ablation rates of glaciers (e.g., Ragettli et al., 2016). However, the presence of permafrost conditions may induce complex interactions with the dynamics of glaciers and debris-covered glaciers (Gärtner-Roer et al., 2022). These factors, associated to the variable ice and water content of the glacial and periglacial landforms, can explain the distinct glacio-geomorphological dynamic responses (Capt et al., 2016; Cusicanqui et al., 2021).

Largely controlled by the debris thickness at the surface, differential ice melt can occur within debris-covered glaciers and in ice-rich permafrost terrains, leading to the formation of lakes, which, in turn, may cause glacial lake outburst floods (GLOFs) (Clague & Evans, 2000; Kääh et al., 2005). In populated mountainous areas, GLOFs can sometimes have catastrophic consequences far downstream (e.g., Emmer et al., 2020). Supraglacial and proglacial lakes are generally easily recognised at an early stage of their formation (Kirschbaum et al., 2019), but technical measures have been taken to mitigate potential hazards only in some cases (Kääh & Haeberli, 2001; Vincent, Garambois, et al., 2010). Conversely, englacial or sub-surface water circulation is more difficult to monitor (Vincent, Auclair, et al., 2010), and it may actively contribute to the dynamics of the thermokarst. On the other hand, in steep mountain terrains, the intensity of flooding can be drastically increased by the slope, the kinetic energy added to the processes and also by cascading effects (Mergili et al., 2020).

The mechanism of thermokarst formation is mainly attributed to thermal and mechanical erosion by water (Harris et al., 2018). In overall cold ice conditions, the water (which may originate from snow and/or ice melt and meteoric precipitation) remains trapped in the thermokarst depression until it can drain away through a surface outlet channel (Haeberli et al., 2001). Conversely, in temperate ice conditions, ice permeability could enhance water infiltration and thus drainage of water can be through an internal conduit (Assier & Evin, 1995; Gulley et al., 2009).

In the southern French Alps, several GLOFs have been documented at the Chauvet glacial and periglacial system (hereafter referred to as 'Chauvet system' in the sake of clarity) since the 1930s, mainly related to the presence of a thermokarst system and an ice gallery (Assier & Evin, 1995). However, very few are known about the origins of these events. The aim of this study is to provide insights into the causes of multiple GLOFs on the Chauvet site. For this purpose, we review historical evidence for the former GLOFs. Then, we analyse long-term glacio-geomorphological changes (volume, surface velocity and internal structure) based on 72 years of photogrammetric data and recent geophysical surveys. Finally, we discuss possible drivers of thermokarst dynamics and of outburst floods.

2 | STUDY SITE

2.1 | General settings

The Chauvet system is located in the upper part of the Ubaye valley in the Southern French Alps (44.85°N, 6.84°E; Figure 1a), in a 1.5-km long west-facing hanging valley at the foot of the western rock face of the *Aiguille de Chambeyron*, altitude 3160 m a.s.l. The Chauvet system ends at ~2710 m a.s.l with a steep front slope covering a steep and narrow bedrock outcrop. The valley has a width ranging from 160 to 450 m and is surrounded by approximately 0.6 km² of densely fractured rock walls (Figure 1b) mainly composed of calcschists and Malm limestone (Chambeyron thrust sheet) (Gidon, 1994; Gidon et al., 1994). At the foot of these highly productive rock walls, debris with a wide range of granulometry accumulate in gravitational scree, which largely feed the glacial and periglacial landforms, such as debris-covered glacier and rock glacier. The high elevation, the predominant north-west orientation and the shadow caused by the >200 m high rock walls surrounding the valley most likely enable permafrost conditions to exist, particularly in the northern exposed areas (Figure 1a).

Based on three previous vertical geoelectrical soundings made by Assier & Evin (1995), the internal structure of the Chauvet system can be roughly assessed. According to these data (located mainly in the central and frontal part of the Chauvet system), it is composed of a 1–4 m thick active layer (resistivities ranging from 4 to 7×10^3 Ohm m), overlaying a 20–40 m thick ice-body and perennially frozen sediments (very high resistivities of 1×10^6 Ohm m) and even a third deeper layer of ice-cemented sediments (with resistivities around 1.5×10^5 Ohm m) (Assier et al., 1994). The presence of ice-rich permafrost is important, as it determines the subsurface thermal conditions, the material properties (including its permeability) around and underneath the thermokarst area and the rheology (e.g., viscous creep and slow degradation).

2.2 | Past outburst floods occurred at the Chauvet system

At least six GLOFs related to the thermokarst lake have been documented since the 1930s, by the Restauration des Terrains en Montagne (RTM, a French national authority in charge of managing natural hazards in mountainous departments). The events are summarised as follows:

- i. The first two GLOFs occurred between 1936 and 1938, and in 1956, respectively. The events are only supported by some testimonies (Assier & Evin, 1995), and hardly identifiable geomorphological traces can be seen on historical aerial images of the middle (2350 m a.s.l) and lower parts (1700 m a.s.l) of the Chauvet valley (Figure S2).
- ii. The third GLOF occurred on 15 July 1970, with 4 h of total drainage time. Evidence collected a few days after suggests that the outburst was accompanied by the collapse of the central elongated depression (hereafter called 'talweg'). Considerable water circulation was observed in the frontal slope (Figures 2a

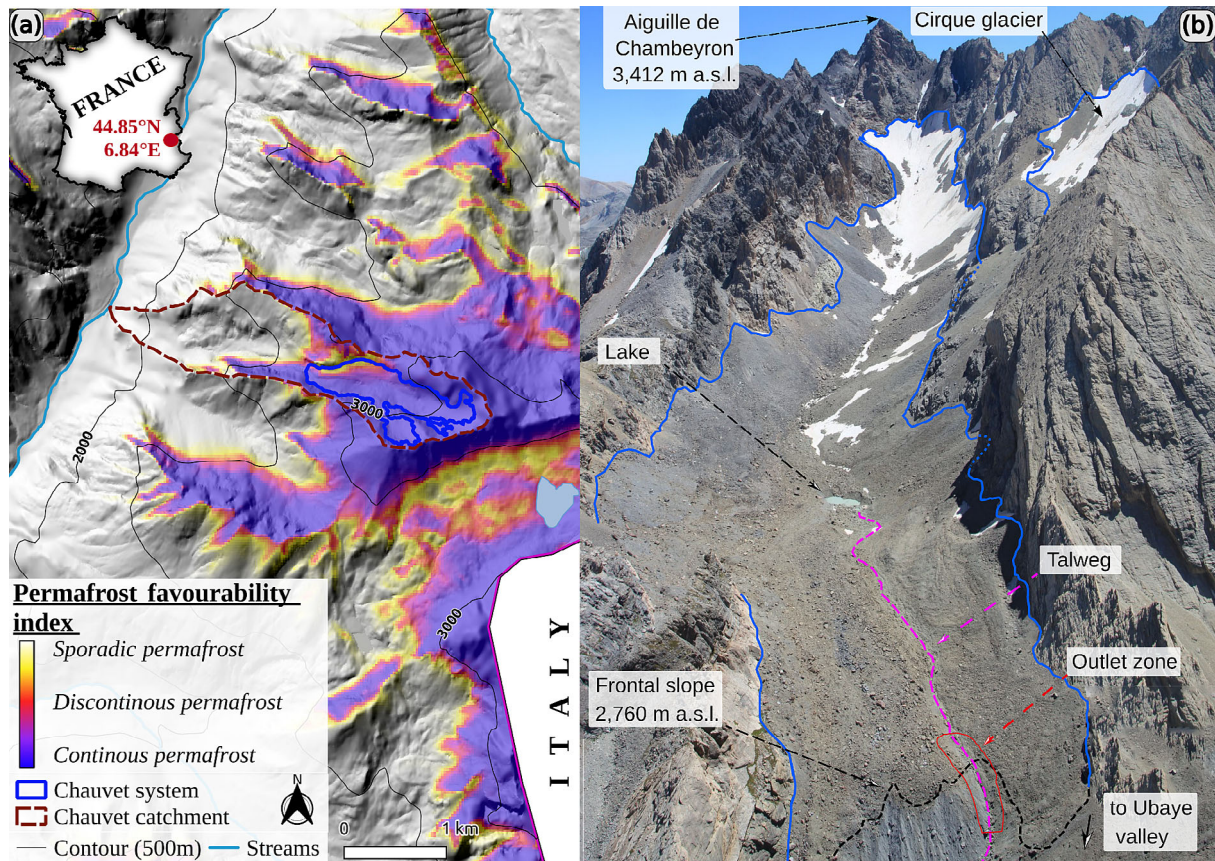


FIGURE 1 Location of the Chauvet system in Ubaye valley, Southern French Alps. (a) The Permafrost Favorability Index (PFI) in the French Alps, according to Marcer et al. (2017). A comparison with the Alpine Permafrost Index Map (APIM; Boeckli et al., 2012) is given in Figure S1. (b) Aerial oblique photograph of the Chauvet system acquired on 7 August 2020 (credits: PGHM, RTM). The blue lines show the extent of the Chauvet system based on image inspection and on observations on the field and on Pléiades high-resolution satellite ortho-images. The pink dashed line shows the talweg (the line of lowest elevation within Chauvet valley), the red polygon shows the outlet zone and the black dashed line shows the frontal slope. [Color figure can be viewed at wileyonlinelibrary.com]

- and S2). Although no precise information is available regarding water or debris volumes, an important amount of sediments was transported according to the geomorphological traces visible on historical aerial images.
- iii. On 16 July 1991, the fourth GLOF happened (drainage time of 90 min). Assier & Evin (1995) reported that the lake drained away through an ‘ice gallery’ (4 m of observed diameter at the entrance; Figures 2b and S4) located in the central part of the Chauvet system (close to 2780 m a.s.l.). These authors mention that the gallery in the subsurface ice (hereafter called conduit) likely continued for about 350 m inside the ice in a down-slope direction. A general collapse of the roof of the conduit occurred after the drainage, revealing massive ice towards the surface (Figure 2). Additionally, water spill-out was observed on the frontal slope in the same zone as during the 1970 event (hereafter called ‘outlet zone’, Figure S9). The volume of water evacuated and debris transported were estimated to be 50 000 m³ and 100–150 000 m³, respectively (Assier, 2018). No significant traces of this event were identified on historical images.
 - iv. The fifth GLOF occurred on 25 July 1997 (3 h of drainage time). Again, the entrance of a 2-m diameter conduit was visible (Figures 2c and S5). Local collapses of the roof of the conduit were observed after the drainage (Figure S5) along with water spill-out in the outlet zone (Figure 2d). The estimated drained

water volume was 70–80 000 m³, and the volume of eroded debris was estimated at around 78 000 m³ (Assier, 2018).

- v. The last and most documented GLOF occurred in two stages on 17 and 21 July 2008 (Figures S6 and S7). The drainage time for the two events was 4.5 and 4 h, respectively. Again, the entrance of the conduit was visible (Figure 2e,f; Figures S6 and S7) and the roof of the conduit almost completely collapsed (resembling an ice crack in Figures 2e and S7). Water spill-out was also observed in the outlet zone (Figures S7 and S9). The estimated volume of drained water during the two events was 90 000 and 16 000 m³, respectively. Little evidence of erosion/deposition suggests that the sediment transport was limited (Assier, 2018).

Although no casualties were reported, impacts of the flooding on the D25 road led the RTM to conduct annual field surveys in late spring of each year to check for the possible formation of a new lake. As reported by the RTM (M. Peyron, 2021, personal communication, April 23, 2021) the lake contains water most of the year, most probably originating from snow and ice melt. Except in the years when a GLOF occurred, water flows of variable intensity were observed in the outlet zone during all the field surveys.

Recent studies conducted by Buckel (2010) and Guibert (2013) investigated the stability of the frontal slope and the potential debris propagation along the Chauvet valley. Their results suggest that in

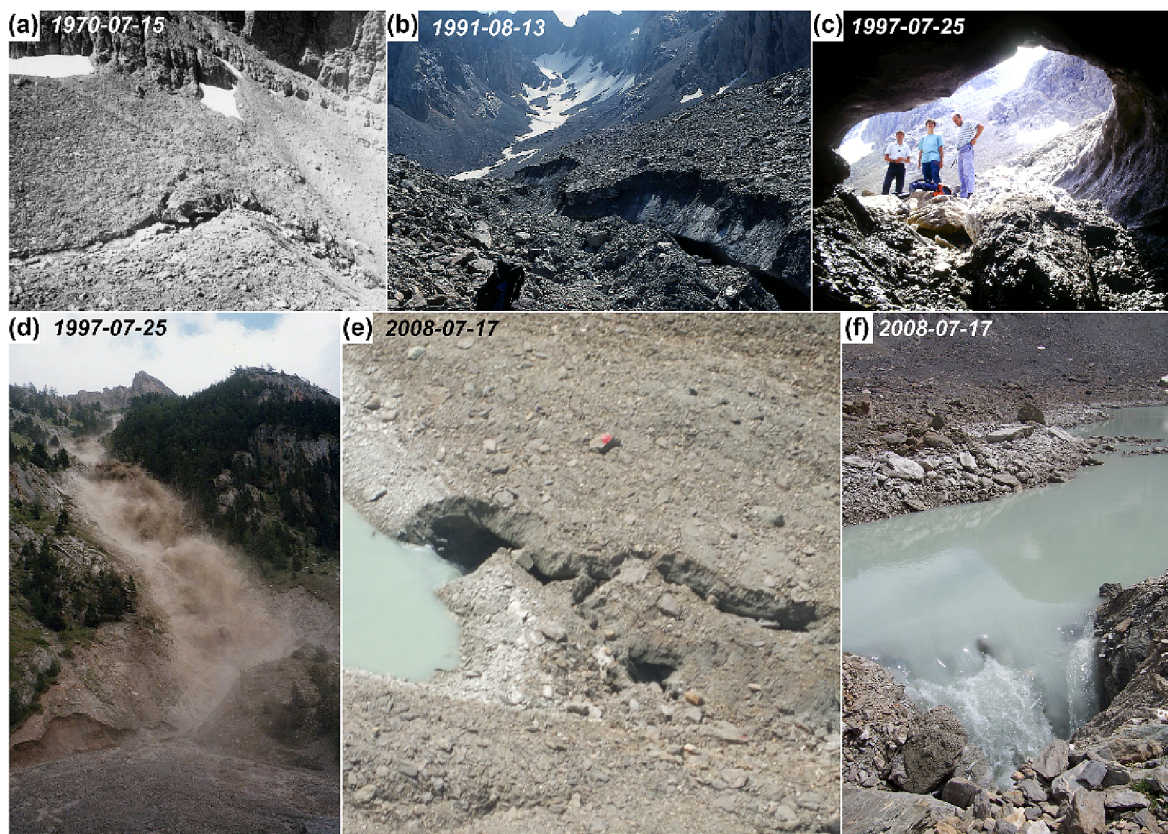


FIGURE 2 Photo-collage summary of the six historical events related to outburst floods of the Chauvet system. (a) Photo of outlet-channel collapse acquired on 15 July 1970 close to glacier frontal slope; (b) photo acquired on 13 August 1991 showing the collapse at lower end of the outlet channel; (c) photo of the tunnel entrance close to thermokarst lake acquired on 2 July 1997, a few days after lake drainage; (d) photo of the Ubaye confluence during water spill-out (1690 m a.s.l.) acquired on 25 July 1997; (e) aerial photograph of the outlet channel collapse at tunnel entrance acquired on 17 July 2008; (f) photo showing water evacuated through the gallery acquired on 17 July 2008. Detailed photographic evidence for each outburst flood can be found in Figures S2–S6. Photo credits: (a) M. Longeron; (b–d) A. Assier and RTM Private collection; and (e and f) PGHM-RTM, M. Peyron [Color figure can be viewed at wileyonlinelibrary.com]

case of flood the amount of destabilised material would likely not be a threat for the Ubaye valley because of the morpho-topographic characteristics below the frontal slope (e.g., the existence of a deposit zone at 2350 m a.s.l.; see Figure S2).

2.3 | Climate settings

The S2M/SAFRAN dataset produced by Météo-France (Vernay et al., 2020) was used to describe the long-term climate changes and the hydro-meteorological conditions that preceded the outburst events during the last 60 years (Figure 3). This part of the Southern French Alps is mainly influenced by a Mediterranean climate, but also by Atlantic disturbances and Eastern atmospheric fluxes. The hydro-meteorological conditions that can be described from the S2M/SAFRAN dataset for the elevation of 2700 m a.s.l. show a mean annual precipitation of 1100 mm a^{-1} (64% corresponding to solid precipitation) without any notable changes in the last 60 years (Figure 3). Nevertheless, a reduction in snow-pack thickness (from 1.5 to 1.0 m) is highlighted from the S2M dataset (Vernay et al., 2020). Regarding temperature evolution (Figure 3), observations at the Col Agnel meteorological station (2630 m a.s.l.; 18.4 km away in Northeast direction) show an important interannual temperature variability around an annual mean of -2.6°C between 1995 and 2020. This suggests that

permafrost conditions are largely present in the Chauvet system, in agreement with the map of permafrost favorability index shown in Figure 1.

3 | METHODS

A multi-disciplinary approach was used combining (i) structure from motion Multi-View Stereo (SfM-MVS) applied to historical and modern aerial photographs and spaceborne images; (ii) geophysical investigations: electrical resistivity tomography (ERT) and induced polarisation (IP); and (iii) geomorphological mapping. These original and complementary datasets allowed us to describe the distribution and characteristics of the subsurface ice and perennially frozen ground, to analyse the spatial and temporal changes in the Chauvet system (surface elevation and flow velocity) and to investigate the dynamics of the thermokarst system.

3.1 | Production of digital surface models and ortho-imagery using SfM-MVS photogrammetry

Our main source of data was the open-access aerial photo library belonging to the French National Institute for Geographic information

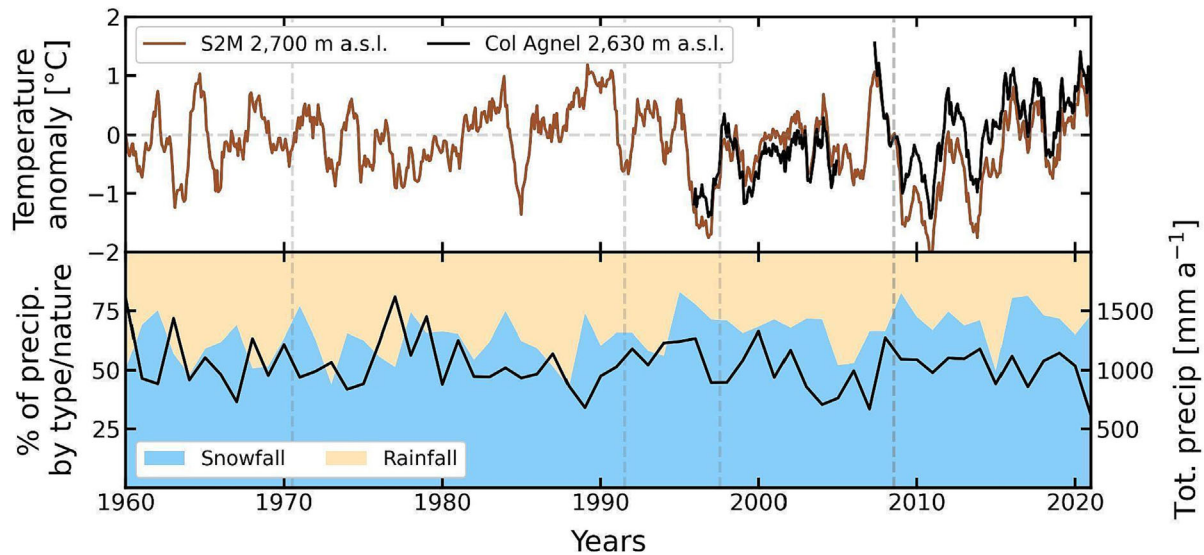


FIGURE 3 Climate settings over the Chauvet system retrieved from the S2M-SAFRAN weather data reanalysis dataset (Vernay et al., 2020). Upper panel shows monthly air temperature anomalies (12 months rolling mean) of S2M dataset corresponding to an elevation of 2700 m a.s.l., a terrain with western exposure and 20° slope in the Ubaye range (brown line) and closest meteorological station ‘Col Agnel 2630 m a.s.l.’ (black line). Lower panel, total annual precipitation in mm, the pale blue and pale orange backgrounds show the respective percentage of solid and liquid precipitation. Grey lines denote outburst flood events. [Color figure can be viewed at [wileyonlinelibrary.com](https://onlinelibrary.wiley.com/doi/10.1002/esp.5650)]

TABLE 1 Details of aerial imagery used as input data settings

#	Acq. date	Δt (a ⁻¹)	No. of photos	No. of GCPs	Type		Ortho/DSM	σ DSM ^a		σ surf. vel.	
					Sensor	Format		(m)	DoD ^b (m)		
1	15-Aug-48	-	3	42	Aerial	Film (B/W)	Yes/Yes	-	-	-	
2	1-Jul-56	7.9	9	42	Aerial	Film (B/W)	Yes/Yes	1.05	-	0.13	
3	4-Sep-73	17.2	18	27	Aerial	Film (B/W)	Yes/Yes	1.59	1.91	0.09	
4	2-Sep-86	13.0	17	41	Aerial	Film (B/W)	Yes/Yes	1.05	1.91	0.08	
5	20-Aug-90	4.0	11	38	Aerial	Film (B/W)	Yes/Yes	1.13	1.54	-	
6	22-Jul-04	13.9	16	39	Aerial	Digital (RGB)	Yes/Yes	0.67	1.31	0.04	
7	19-Jul-09	5	16	41	Aerial	Digital (RGB)	Yes/Yes	-	0.93	0.13	
8	2-Oct-12	3.2	39	42	Aerial	Digital (RGB)	Yes/Yes	0.65	0.92	0.20	
9	3-Jun-15	2.7	1	-	Aerial	Digital (RGB)	Yes/No	-	-	0.34	
10	15-Sep-18	3.3	1	-	Aerial	Digital (RGB)	Yes/No	-	-	0.23	
11	9-Aug-20	1.9	2 ^c	8 ^d	Satellite	Digital (RGB/Pan)	Yes/Yes	0.6	0.88	0.08	
12	18-Aug-20		700	11(6 ^e)	Drone	Digital (RGB)	Yes/Yes	-	1.21	-	
Average								0.96	1.34	0.11	0.2

Note: The reference dataset used for co-registration of DSMs is in bold.

^aValues after co-registration.

^bCumulative uncertainty.

^cStereo acquisition.

^dAdditional correction using RPC.

^eGCP deployed into Chauvet system.

(French acronym **IGN**) and its online tool ‘**Remonter le temps** (back in time)’, which contains scanned images of historical aerial photographs from 1948 to 2013. Table 1 lists the nine campaigns used in this study. Digital surface models (DSMs) and ortho-images were produced using SfM-MVS techniques with Agisoft Metashape software (version 1.6) (Smith, 2011). This methodology performs well in DSM production using historical aerial photographs in high-alpine environments (e.g., Cusicanqui et al., 2021; Mertes et al., 2017; Westoby et al., 2012).

We selected ground control points (GCPs) coordinates from the IGN Web Mapping Service (WMS) (Rodríguez et al., 2008), using easily identifiable features (e.g., boulders) visible on recent high-resolution images of stable areas outside the Chauvet system. We were able to use the same set of 20 GCPs (Table 1) for all the surveys. For the elevation of the GCPs, we used a reference DSM from IGN **RGE ALTI-5m** (± 5 m of uncertainty over flat areas) to extract this information. Finally, all SfM-MVS derived DSMs and ortho-images were resampled to 1-m horizontal resolution to allow easy comparison.

An UAV survey was performed using a Phantom 4 RTK on 17 August 2020, covering the entire Chauvet system. Independent GCPs were measured using a rover (Trimble Geo7x GNSS receiver) and a local base station (GB1000 Topcon) located 1 km farther down valley. We also used two stations of the IGN Permanent GNSS Network (*Réseau GNSS Permanent*, RGP) for GCPs post-processing. Vertical and horizontal uncertainties less than 0.1 m were found for all GCPs. The UAV DSM was resampled to 1 m resolution (to be consistent with the ones derived from aerial photographs), in addition to the original 20-cm resolution DSM.

To complete the set of images and to obtain broader spatial coverage than the UAV (Table 1), a pair of sub-metric optical stereo-images from the Pléiades constellation (CNES, Airbus D&S) was acquired over the entire Ubaye valley on 9 August 2020. The Pléiades-derived DSM and ortho-images at 1 and 0.5 m resolution, respectively, were processed with the Ames Stereo Pipeline (ASP) workflow (Shean et al., 2016) using rational polynomial coefficients (RPCs) and eight independent GCPs distributed over the entire image and measured with a differential GNSS (Trimble Geo7X as a rover and four GNSS base stations from the permanent IGN-RGP network).

We performed a supplementary 'co-registration' in order to reduce uncertainties (e.g., Cusicanqui et al., 2021). We used the Iterative Closest Point (ICP) methodology proposed by Besl & McKay (1992) within Shean et al. (2016) workflow. The 2009-DSM presents the best characteristics in terms of geometry (low B/H ratio, radial distortions of photographs), snow-free cover, shadows and surface reconstruction. It was used as a reference to align the other DSMs. The area used for co-registration covers 3.11 km², which accounts for 21% of the DSMs (Figure S10). Finally, the ortho-images were also shifted using the values given by the alignment for each respective DSM (Table S1).

3.2 | Changes in surface elevation

We used the Difference of the DSM's (DoD) metric to evaluate changes at the surface of the Chauvet system. For this purpose, we used the co-registered 1-m DSMs for six sub-periods (Figure S11; Table 1, excluding 1948 and 1990 due to poor quality). The uncertainty of the DSMs was estimated using root mean square deviation for each pair of DSM (RMSE; Wheaton et al., 2010) on the stable terrain outside the Chauvet system and in the surrounding valleys (Figure S10). The uncertainties were computed using the 2009 reference DSM for each DSM, yielding an overall average value of 1.3 m (specific uncertainties are listed in Table 1).

3.3 | Computing horizontal surface displacements

We computed 2D surface displacements from feature tracking image correlation techniques using IMCORR algorithm in SAGA GIS software (Conrad et al., 2015; Scambos et al., 1992). After various tests, the following parameters were selected for the feature tracking stage: search chip size = 64 pixels, pattern chip size = 32 pixels and grid interval = 10 pixels. Next, a two-step filtering procedure was applied to the correlation points, with the removal of, first, the points in the thermokarst lake area as well as in the snow/shadow areas

(incoherent correlation points) and, second, of noisy values following the criteria of flow direction and anomalous displacement values. Once filtered, the correlation points were interpolated onto a 5-m resolution grid using an inverse distance weighted method (Figure S12). Finally, we computed surface displacement uncertainties using feature-tracking correlation points based on the same stable areas as those used for the DSM co-registration process around the Chauvet system (Figure S10). Here again, we masked the correlation points located over a slope of >30° as well as snow covered/shadowed areas that presented noisy values.

3.4 | Geoelectrical survey

ERT tomography has been broadly used to detect and monitor mountain permafrost in the past 30 years (e.g., Kneisel, 2006; Mollaret et al., 2019) including in both rock glaciers with 2.5-D and 3D inversion algorithms (e.g., Duvillard et al., 2018; Maurer & Hauck, 2007) and debris-covered glaciers (Bosson et al., 2015). The conductivity (inverse of the resistivity) describes the ability of a rock to conduct an electrical current when an electrical field is applied to the material. It can be measured with quadrupoles, two electrodes being used to inject and retrieve the current and two electrodes (or more) used to measure a difference of electrical potential (i.e., a component of the electrical field) at the ground surface. In addition to classical ERT techniques, induced polarisation (IP) has been recently used to confirm the presence of ice and permafrost (Abdulsamad et al., 2019; Duvillard et al., 2021). Induced polarisation is a natural extension of ERT and can be performed with the same equipment and in the same time frame than ERT. IP can be related to the properties of the electrical double layer coating the surface of the grains (Kemna et al., 2012; Revil et al., 2020). The chargeability measured in induced polarisation surveys characterises the ability of a rock to store reversibly electrical charges when submitted to an electrical current.

ERT and IP surveys were carried out on 17–21 September 2020. During the field campaign, four transverse profiles (5-m electrode spacing; Table 2) were performed downward with respect to the thermokarst zone (Figures 4 and S13). Furthermore, a 1600-m long longitudinal profile (20-m electrode spacing; Table 2) was carried out across the thermokarst zone and the thermokarst lake, passing through the frontal slope and ending 160 m further down valley (see position in Figure 4). We used 10-mm thick and 40-cm long stainless steel electrodes. During the acquisition, we used salty muddy bentonite to improve the electrical contacts between the electrodes and the ground (Maurer & Hauck, 2007), and the different cables were connected to an ABEM Terrameter SAS-4000 resistivity meter. We used the standard Wenner configuration for all the acquisitions because of its good signal-to-noise ratio in complex areas like inside rock glaciers (Dahlin & Zhou, 2004; Kneisel, 2006; Revil et al., 2010). Electrode coordinates were measured using a differential GNSS (Trimble Geo7X) with a 2-cm accuracy and post-processed using the RGP-GNSS network. The ERT and IP data were then inverted in RES2DINV 3.54.44 software using a smoothness-constrained least squares method and the Gauss-Newton method (Loke & Barker, 1996). The ERT and IP datasets are expressed in terms of resistivity (in Ohm m) or conductivity (S m⁻¹) and normalised chargeability (S m⁻¹). Then, the final tomogram (obtained once a convergence criterion is reached in the

TABLE 2 Electrical resistivity and induced polarisation survey profiles

Profile	1	2	3	4	5
Spacing between electrodes (m)	5	5	5	5	20
Number of data points surveyed	453	471	443	257	270
Number of electrodes excluded	-	-	61–62	45–46	53
Number of inverted points	415	436	429	215	238
ER root-mean-square error	15.4	6.3	10.2	8.5	11.3
IP root-mean-square error	2.7	1.9	8	8	1.1

Abbreviations: ER, electrical resistivity; IP, induced polarisation.

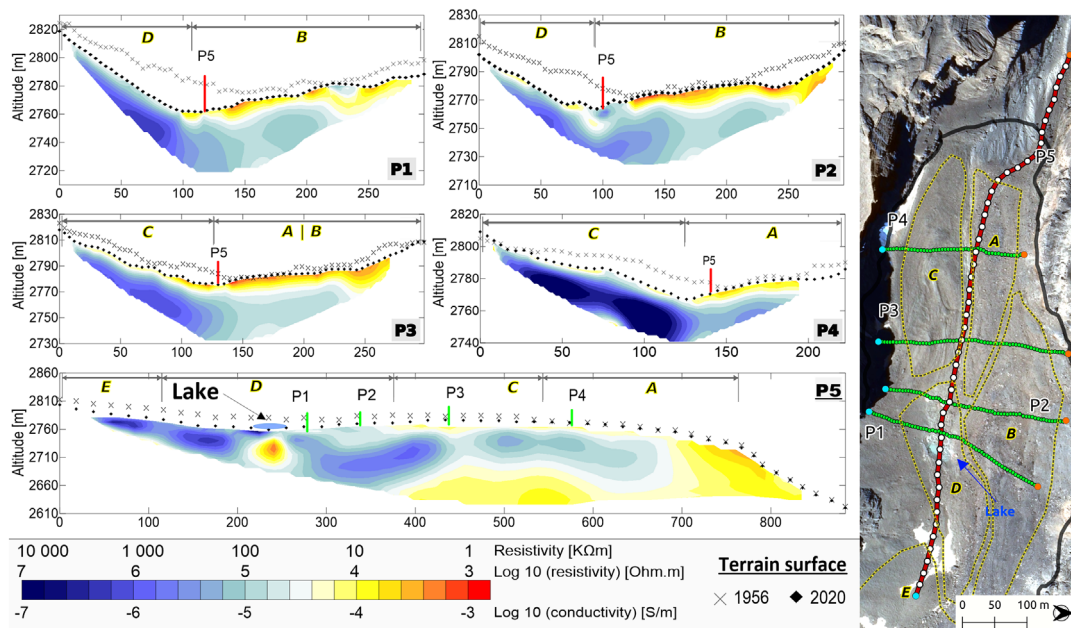


FIGURE 4 Geoelectrical resistivity tomograms of the Chauvet system. ‘Profiles 1 to 4’ correspond to transverse profiles acquired between the lake and the rock glacier front (green lines on the map) with 5 m spacing between electrodes. ‘Profile 5’ corresponds to a large-scale geoelectrical profile acquired between 200 m above the lake down to 150 m beyond the rock glacier frontal slope (red line on the map) with 20 m spacing between electrodes. In the profiles, the lines of Xs and the dotted lines correspond to the surface elevation of the glacier in 1956 and 2020, respectively, and the yellow letters correspond to geomorphological sector on the map. The number of data points and inversion error are listed in Table 2, and electrical chargeability tomograms in $S\ m^{-1}$ are shown in Figure S13. [Color figure can be viewed at wileyonlinelibrary.com]

iterative inversion of the apparent resistivity and chargeability data) can be interpreted with the dedicated petrophysical model developed in Coperey et al. (2019).

3.5 | Geomorphological mapping

Based on field observations as well as on data derived from our dataset, a detailed geomorphological map of the Chauvet system was produced. We used the UNIL legend (Lambiel et al., 2016; Schoeneich, 1993) adapted to account for the different glacio-geomorphological features of the area. A field survey was undertaken from 17 to 19 August 2020, based on printed 1-m resolution aerial orthophotos and shaded relief maps. The geomorphological features were then digitised on QGIS software using the very high resolution UAV-derived ortho-image and hillshade DSM to refine details (Section 3.1). To identify the nature and the activity levels of the processes that presently shape the Chauvet system, we used the results from the geophysical survey and the multi-temporal products from

the photogrammetric approach (ortho-images and hillshaded DSM from 2009 to 2020) to better identify and delineate the landforms.

In addition, different positions of thermokarst lakes and of the talweg were observed over time. We digitised their positions for each year where ortho-images and DSMs made this possible. The thermokarst depressions were delineated following their upper edge (Figure S14). Likewise, the talweg was always digitised from the rock outcrop (located in the frontal slope sector) up to the thermokarst lake. This mapping procedure allowed us to estimate the horizontal and vertical displacements of talweg for eight sub-periods.

4 | RESULTS

We first present the data on the internal structure (Section 4.1), then the changes in surface elevation (Section 4.2) and finally the surface displacements (Section 4.3). They serve as a base to define and delineate the glacio-geomorphological units (sectors A–E) presented in Section 4.4 (Figure 7) and to assess their dynamics.

4.1 | Internal structure

Figures 4 and S13 show geo-electrical conductivity/resistivity and normalised chargeability tomograms, respectively. Looking at the transverse profiles (P1–P4 in Figure 4), a clear pattern of differentiated resistivity values appears between the left- and right-hand side of the Chauvet system. Indeed, the left orographic side (sector C) shows very high resistivity values (0.1 to 1×10^7 Ohm m), indicative of probably massive ice, covered by a thin 1–2 m layer of debris (left side in Figure 4), whereas the right orographic side (sectors B and C) has mainly lower resistivity values (around 1×10^5 Ohm m) more typical of frozen sediments, buried below a 3–6 m layer of unfrozen debris (locally reaching 15 m depth with resistivities ranging from 0.1 to 1×10^4 Ohm m).

As also confirmed by field observations (for instance along the sub-vertical ice-cliff bordering the thermokarst lake), remnants of massive ice of about 20–40 m thickness (high resistivity above 1×10^7 Ohm m) can be seen on tomogram P5 (between 25 and 200 m along the profile), upslope of the thermokarst depression where the lake is currently located, and continuing downslope from the lake down to the transverse profile P3 (Figure 4). On P5, at a depth of 40–70 m between P3 and P4, resistivities lower than 1×10^4 Ohm m can be interpreted either as a layer of frozen debris or as the bedrock. According to Coperey et al. (2019), values below the 2.5×10^4 Ohm m threshold have been chosen to discriminate unfrozen materials. In this same section, the ice-reach terrain appears to be thinner and likely less homogeneous. Further down, following the P5 longitudinal profile below P4, the resistivity decreases gradually until the frontal slope. Between 700 and 850 m on P5, resistivities

lower than 1×10^4 Ohm m have again been measured, corresponding likely to unfrozen sediments.

Features probably related to the presence of interstitial liquid water are visible, with lower resistivity values (0.1 to 1×10^4 Ohm m), until a depth of 20 m below the lake on P5 and at about 5 m depth on P2, at the location of the conduit. Regarding this later point, it was possible to hear water circulating underneath the debris layer (even though no water was visible at the surface) during the field campaigns in August and September 2020.

4.2 | Changes in surface elevation

Changes in thickness across the Chauvet system are expressed as annual average thickness changes for the six sub-periods between 1956 and 2020 as well as the absolute changes over the entire 1956–2020 period (Figures 5 and S11). Because the interest mainly relies on the dynamics of the thermokarst lake, but also because snow and shadow often alter the quality of photogrammetric data on the upper part of the Chauvet system, we focus on the results for the central and lower part of the Chauvet system, roughly from the middle part of sector E (2900 m a.s.l.) down to the frontal slope (Figure 5a). Once the vertical changes within the limits of detection were removed (0.1 m a^{-1} on average over the period 1956–2020, Figure 5b), some patterns can be seen relatively stable both in space and over the whole period investigated.

Regarding spatial patterns, the highest thinning rates ($-1.1 \pm 0.1 \text{ m a}^{-1}$, Figure 5) are found in the lower part of sector E at 2800 m a.s.l. and above, with a mean total absolute change in

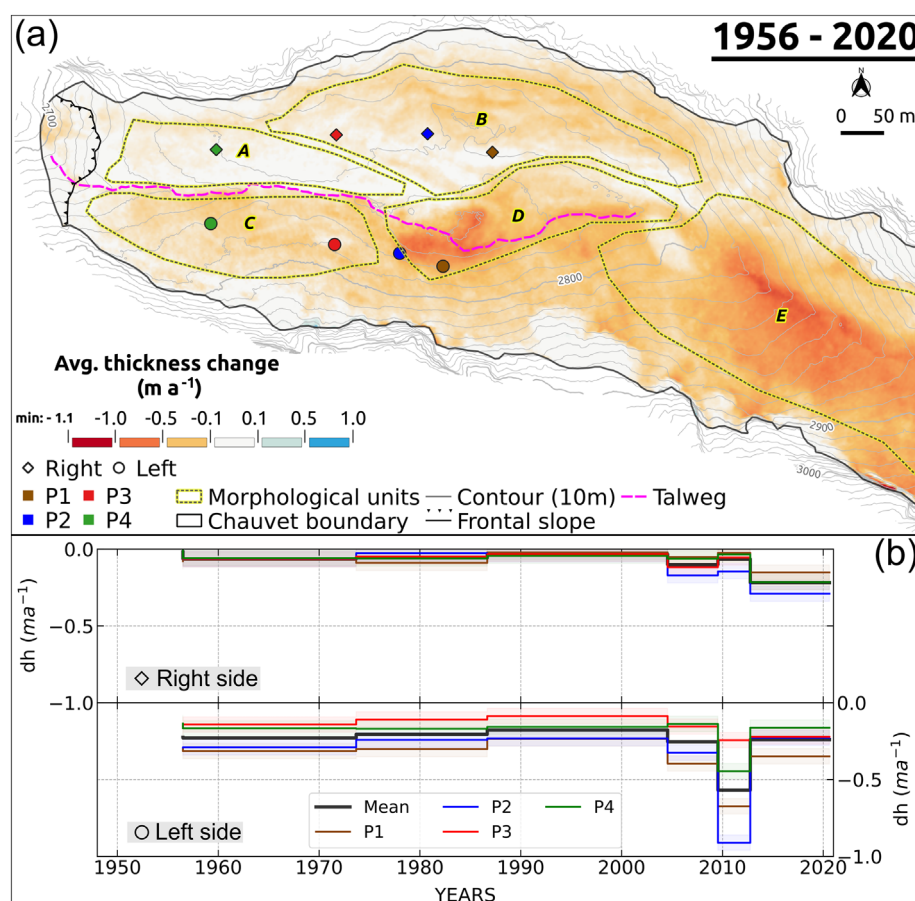


FIGURE 5 Spatio-temporal vertical changes in the Chauvet system in the period 1956–2020 (computed from the six periods listed in Figure S11). (a) The background colour-gradient reveals averaged changes in thickness over the entire period. The areas surrounded by the yellow-dotted lines correspond to the morphological units delimited in Section 3.5. (b) The vertical changes over time for each of the coloured circles and diamonds in (a) as well as the mean of all the points. Coloured boxes correspond to the uncertainties (see Table 1 for details). [Color figure can be viewed at wileyonlinelibrary.com]

thickness of -18 ± 1.3 m over this area (Figure S11). Then, sector *D* is the second sector the most affected by thinning (-0.75 ± 0.1 m a^{-1}) but with less varying spatio-temporal patterns (mean total loss of -15 ± 1.3 m for the area). Surface changes are stronger on sector *C* than on sector *B*, with similar thinning rates ranging from -0.3 to -0.5 m a^{-1} (corresponding to variations of -11 to -8.5 ± 1.3 m in surface elevation) over the entire 1956–2020 period. Alternating linear patterns of small and large vertical changes are found in sectors *A* and *B*, most probably indicating displacements of the ridges down-slope. Positive elevation changes (i.e., 2009–2012 period; Figure S11) in sector *B* near sector *D* likely support some back-creeping displacements. On sector *A*, limited thinning rates of -0.15 m a^{-1} (-3 ± 1.3 m of lowering of the surface) are rather homogeneously distributed. Local surface lowering is observed along the talweg in different periods: in the 1956–1973 period near to the frontal slope; in the 1986–2004 period in the median section of sector *A*; and in the 2004–2009 period, when several parts are affected (Figure S11).

Regarding temporal patterns, we reconstructed spatially averaged (over an area with a radius of 20 m) time series at eight sites (four on the left and four on the right orographic side) located at the ends of the four ERT transverse profiles approximately in the centre of sectors *C*, *B* and *A* (Figure 5a). Rather low but constant thinning rates reaching -0.2 m a^{-1} for sector *C* and -0.05 m a^{-1} for sectors *A* and *B* are observed during the first periods (1956–1973, 1973–1986 and 1986–2004). Subsequently, the surface lowering pattern is contrasted on the left- and right-hand side of the landform. On the left-hand side, an increase in surface lowering is identified between 2009 and 2012 compared to the previous period. On the right-hand side, the increase

in surface lowering occurs stepwise and the highest values are reached after 2012 (multiplied by factors of 2).

Regarding changes in the thermokarst lake, intermittent behaviour and low thinning rates are observed between 1956 and 2004 (an average of -0.2 m a^{-1} for this period; Figure S10). From 2004 until 2012 (see Figure S10), high thinning rates are observed in sector *D* (an average of -1.1 m a^{-1} for the entire period). During the last period 2012–2020 (Figure S11), very localised variations in thickness are observed in sector *D*, likely linked to the ice cliff and to the formation of the thermokarst lake. Additionally, in the same period, a general lowering of the surface characterised the Chauvet system with slight thinning -0.2 m a^{-1} . However, over the talweg, the thinning rates are reduced (i.e., within limits of detection).

4.3 | Surface displacements

The spatial distribution of the surface displacements was reconstructed for 10 sub-periods (1948–2020; Figure S12), and the surface velocity patterns were averaged over the whole 1948–2020 period (Figure 6) for the lower half part of the Chauvet system. Looking at general spatial patterns, we note that sector *E* presents the highest velocities of the entire study period (>1.5 m a^{-1}). In the vicinity of sector *D*, the ice fluxes converge towards the depression. Down-slope, fluxes converge towards the talweg, almost perpendicular to the general E-W orientation of the valley. Sector *C* has slightly higher average velocities (0.5 ± 0.2 m a^{-1}) than sector *A* (0.25 ± 0.2 m a^{-1}). In the contact zone between sectors *A* and *B*, the ice fluxes diverge

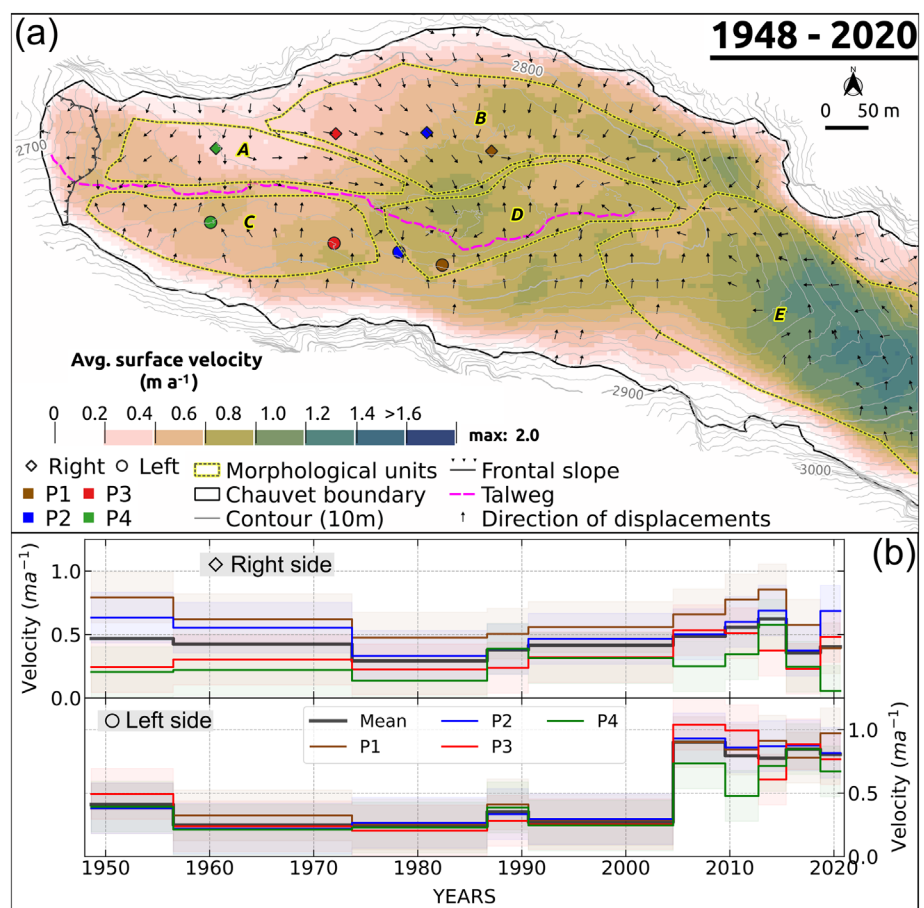


FIGURE 6 Averaged surface velocities of the Chauvet system for the period 1948–2020. (a) The background colour gradient shows spatially averaged surface velocities computed for 10 sub-periods (the detailed sub-periods are reported in Figure S12). This panel also shows the averaged potential direction of the displacements (black arrows) and the position (extension, pink dotted line) of the talweg in 2020. The coloured circles and diamonds (left and right hand side, respectively) show the position from which averaged values were computed (20-m radius around each point). These points are located over geo-electrical profiles (Figure 4). (b) Changes in surface velocities over time for each circle and diamond as well as the mean of all the points [Color figure can be viewed at wileyonlinelibrary.com]

towards the frontal slope sector to the west and towards the central depression to the east.

Regarding the spatio-temporal patterns of the surface displacements, on average, the two orographic sides of the area of interest display rather similar orders of magnitude ($0.5 \pm 0.2 \text{ m a}^{-1}$; Figure 6), but with different spatial variability, the behaviour observed on sector C is more homogeneous than on sectors A and B. The highest surface velocities (2.0 and 1.2 m a^{-1}) are observed in sectors E and B, respectively, in the first sub-period 1948–1956 (Figure S12), in contrast to the slow movements observed in sectors A and C ($0.3 \pm 0.2 \text{ m a}^{-1}$). This spatial pattern is repeated in the four following sub-periods but with lower values (by a factor of 3) in sectors C E (Figure S12).

Remarkable changes occurred on sector C after 2004, where the surface flow velocities increased drastically to $1.0 \pm 0.2 \text{ m a}^{-1}$, whereas the increase was more progressive on sectors A and B starting in the late 1990s. On the latter landforms, maximum surface displacement values of the observational period were reached in the 2012–2015 period, whereas the peak, although not as clear as for sectors A and B, is reached between 2004 and 2009 on sector C (0.6 m a^{-1} ; Figure 6b). Between 2004 and 2015, a well-marked acceleration over sectors D and E was observed ($+0.2 \text{ m a}^{-1}$ with respect to the previous period). In the last two sub-periods, slower surface velocities are found on the right-orographic units (sectors A and B), with a clear decrease between 2015 and 2018 followed by an increase between 2018 and 2020, whereas the central part of sector A is almost unchanged. In sector A, a slowdown is observed even to the point of being stable (but still within the limits of detection) for the last period

2018–2020 (Figure S12). In contrast, sector C does not show similar behaviour; this sector remains stable with velocities roughly the same since the increase in 2004 (Figures 6 and S12).

4.4 | Glacio-geomorphological analysis

The detailed geomorphological field analysis, together with the results of geophysical survey and of the topographical changes, provides keys to understand the glacio-geomorphological dynamics and their spatial relationships within the Chauvet system. The proposed interpretation is synthetized in the geomorphological map (Figure 7) and allows the definition of six main morphological units:

- i. Sector E occupies most of the upper reach of the valley, between 3100 and 2800 m a.s.l. This sector is nowadays entirely covered with debris and presents spatially homogeneous high thinning rates ($-1.1 \pm 0.1 \text{ m a}^{-1}$; Figure 5). Although no ice is currently visible at the surface, massive ice and crevasses can be clearly seen in the photographs dating from 1898, 1948, 1956, 1973, 1994 and 2004 (see Figure S15). Field observations by Assier & Evin (1995) and the present study suggest that the thickness of the debris layer is currently between 0.6 and 1 m. According to the resistivity values (above $1 \times 10^6 \text{ Ohm m}$), the lower part of this sector, that is, the closest one from the thermokarst lake, is mostly occupied by remnants of massive ice, very likely from glacial origin. Snow patches regularly cover sector E and the

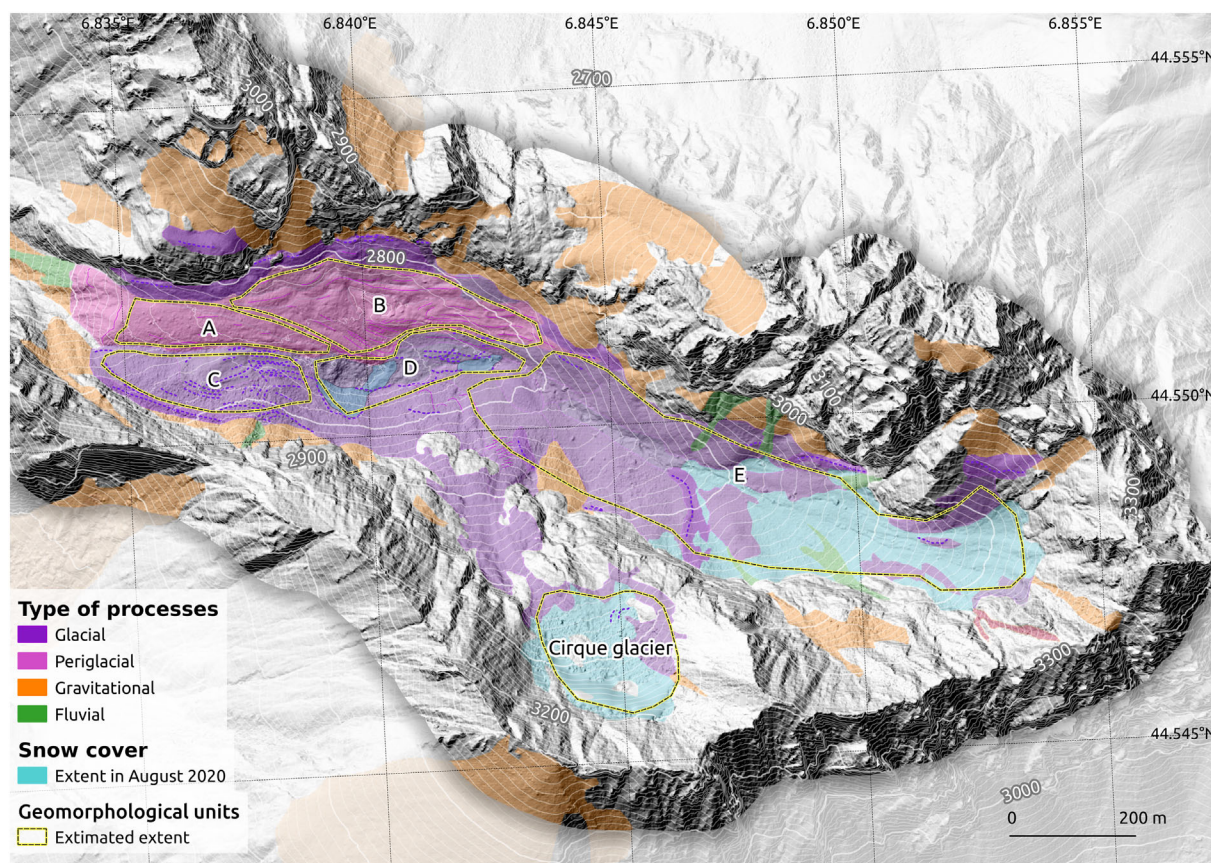


FIGURE 7 Glacio-geomorphological context of the Chauvet system, according to its status in late summer 2020. The morphological units delineate the main zones discussed in this same section. [Color figure can be viewed at [wileyonlinelibrary.com](https://onlinelibrary.wiley.com)]

- resistivity tomogram P5 stops at 2810 m a.s.l. (500 m up-valley from the lake); therefore, only the lower part of this sector can be interpreted, and further geophysical measurements are needed to be able to conclude about the status of this sector, as a debris-covered glacier of a dead-ice landform.
- ii. A *cirque glacier* on the left-orographic side of the Chauvet valley is located on a small hanging cirque between 3200 and 3000 m a.s.l. The 1854 old military map (Carte d'Etat Major in French) and the photograph taken in 1898 (Figure S15) suggest that this glacier was connected to the main glacier at around 2900–2850 m a.s.l. during the LIA. Ice and crevasses were clearly visible on aerial photographs from 1990, and today, some remnants of massive ice are probably present in this sector but are completely covered by debris. The former connexion during LIA or similar extensions may however explain some observed differences in the lower part of the system in terms of shape, nature, content and characteristics of the ice and thickness of debris cover between the right side (fed by *sector E*) and the left side (fed by the clean cirque glacier). We did not include this sector in our analysis because it is not anymore connected to the main system.
 - iii. The *thermokarst area* (*sector D*; Figures 7 and S7) is characterised by a topographic depression in the middle of the watershed where the lakes form (observed since 1948; Figure S15). The lake develops between massive ice (likely from glacial origin) as well as frozen debris. Massive ice is clearly visible along the ice-cliff on the southern side of the main depression (Figure S8) and detectable at the distance ~0–200 m on the resistivity tomogram (resistivities above 1×10^6 Ohm m). Additionally, the resistivity tomograms P1 and P2 exhibit the presence of massive ice is detectable at the distance ~0–130 m on the left orographic side of the depression. Furthermore, frozen debris (resistivities around 1×10^5 Ohm m) at the opposite side of the depression (*sector B*).
 - iv. On the northern side of the Chauvet system (right orographic side of the thermokarst area) the topography shows E-W oriented ridges and steps, suggesting creeping of frozen sediments and/or the sliding of slabs of frozen terrain towards the thermokarst depression along a mean slope of 16° (*sector B* in Figure 7). Resistivity values (around 1×10^5 Ohm m) suggest the presence of perennially frozen sediments. Gravitational readjustment of this sector was probably induced by the lowering of the thermokarst depression, explaining the longitudinal steps observed in the landscape.

Between the thermokarst area (*sector D*) and the frontal slope, the so-called 'talweg' (see Section 2.2.) splits the valley bottom into two lateral parts (Figure 1b). It is clearly identifiable since 1948 and separates two areas with well-marked morphological asymmetry:

- v. The left-orographic side of the valley between 2800 and 2750 m a.s.l. (*sector C* in Figure 7) is characterised by rather simple morphology with a large flat area and arcuate or linear ridges several metres in height and several tens of metres in length; it covers 2/3 of the area. The surface granulometry consists of smaller blocks than the right-orographic side with large quantities of fine sediments and the mean slope is 22° (Figure S8).

Geoelectrical profiles show very high resistivity values (between 0.1 to 1×10^7 Ohm m), under a thin debris layer. The surface topography shows a distinct lateral movement following local slope inclination towards the talweg and a significant surface lowering. We interpret this sector as a massive ice body, which may have been deposited by the former Chauvet glacier and the cirque glacier. The surface lowering reveals massive ice-loss. The arcuate ridge and furrow topography are consistent with the creeping towards the talweg (Figure 6).

- vi. On the right-orographic side (*sector A* on Figure 7), a bulging/convex surface area extends between *sector D* and a well-marked frontal slope (40° slope) at 2710 m a.s.l. Resistivity values are lower than on the opposite side (around 1×10^5 Ohm m), indicating frozen sediments, covered by a thick unfrozen layer. Surface movements appear to be low and very dispersed in direction, whereas the surface lowering is less pronounced. All these elements suggest an ice-debris mixture typically found in ice-rich permafrost terrain. It could be interpreted as a rock glacier or as an interlayered ice and debris complex. The position of the frontal slope appears to be stable, controlled by the underlying slope break in the bedrock (Figure S8), and delivers debris to the steep ravine system immediately downstream.

Lateral moraines at similar elevation can be observed on both sides of the lower part of the system. On the orographic left side, a long and sharp lateral moraine crest is deposited on the top of *sector C*. It is separated from the rock wall by a narrow depression, in which short talus cones and snow patches accumulate. On the orographic right side, a somewhat indistinct moraine complex dominates back-creeping *sector B*. Further downvalley and still on the orographic right side, a short lateral moraine is preserved on the bedrock above the edge of *sector A* and ends just above the frontal slope.

4.5 | Spatio-temporal dynamics of the thermokarst lakes and talweg

Among the elements that stand out over time, the migration of the talweg and the thermokarst lake are the most striking. The talweg migrated in a general southward direction, in a more pronounced way in the vicinity of the thermokarst depression where it migrated horizontally more than 50 m. The magnitude of the migration gradually decreases approaching the frontal slope where it does not exceed 15 m (Figures 8b and S14). Although the preferential direction of migration is southward, an inverse pattern is observed on each transverse profile during the most recent period (2013–2020) where the direction of migration abruptly turned northwards in all cases, reaching 10 m for P1 and 2 m for P3 (Figure 8b). The thinning rates at the location of the talweg present the same pattern with strong negative vertical changes in *sector D* and less pronounced changes (-50%) close to the frontal slope (reaching, respectively, -2.5 and -1.2 m a^{-1}). The thinning rates became much more pronounced after 2004 (Figure 5).

The behaviour of the thermokarst sector differs slightly from that of the talweg. From 1948 to 1990, lakes developed intermittently (new small lakes appeared and disappeared), all migrating mainly south-westwards. After 2004, a single lake was present at the surface,

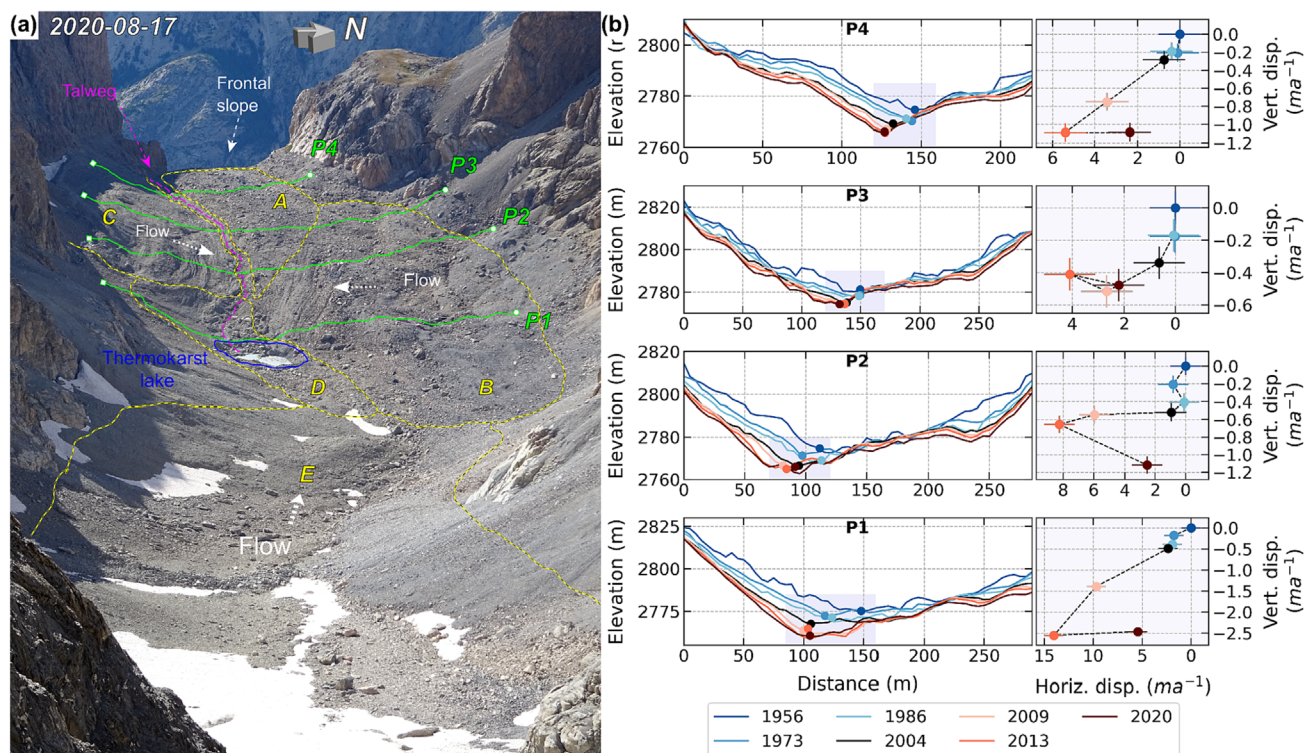


FIGURE 8 (a) Terrestrial photograph taken on 17 August 2020, from the ‘Col de Chambeyron’ (3280 m a.s.l.) with a view over the Chauvet system. The white arrows denote the potential flow direction; the green lines denote the position of the ERT profiles (Figure 4 and Section 3.4), and the pink line denotes the position of the talweg; yellow-black dashed lines indicate the morphological units defined in Section 3.5. (b) The panels on the right show the diachronic profiles along each ERT acquisition with the surface elevation profiles for eight available DSMs (Table 1). In the centre of profiles P1 to P4, the pale blue square contains dots that correspond to the talweg displacement. The panels on the right are close-ups of the pale blue squares showing cumulative horizontal displacements versus cumulative changes in the elevation of the outlet-channel using, respectively. DSM and ortho-image acquired in 1956 as references [Color figure can be viewed at [wileyonlinelibrary.com](https://onlinelibrary.wiley.com)]

but this time, it migrated in the opposite direction (south-eastwards) while increasing in surface area (Figure S14). In agreement with Assier & Evin (1995), we hypothesise that the talweg and thermokarst lake are connected below the debris layer because the same pattern of migration is reflected in the entrance to the conduit, still in a south-westerly direction for 10 to 20 m (Figure S9). Conversely, the same pattern is not observed at the conduit outlet, which remains stable over time. This area has not undergone any drastic movements.

5 | DISCUSSION

5.1 | Changes in the glacio-geomorphological system since late-LIA

During the LIA, glaciers in the Southern French Alps (Haute-Ubaye valley, Queyras and Mercantour national parks) occupied a total area of 1.57 km² (Gardent, 2014). Since then, glacier area has reduced to 0.56 km² in 1996 and to ~0.25 km² in 2015, divided into three glaciers. Nowadays, ~80% of the remaining glacierized area is debris covered (Gardent, 2014). Based on the currently still existing massive ice bodies in the Chauvet system (Figures 4 and 9) and the glacio-geomorphological interpretations (Section 4.4), it is very likely that (i) the upper Chauvet valley (above 2740 m a.s.l.) was largely covered by a glacier during the LIA and that (ii) two branches, the North-facing cirque glacier and the main West-facing Chauvet glacier (now sector E),

were merging near the present thermokarst area (sector D). These assumptions are supported by historical photographs taken in 1898 or the ‘Carte d’Etat Major’ map dated to 1854 from the French *Service géographique de l’Armée* (IGN, 2021; Figure S15) and by the presence of lateral moraines on both sides of the valley at 2780 to 2800 m a.s.l. near the frontal slope (see Section 4.4 and Figure 7). These moraines are approximately at the same elevation and could indicate the ice level reached during the LIA. Either the LIA glacier might have overridden previously existing dead ice bodies (sectors A and C) or these bodies are remnants of the LIA glacier activity. Evin & de Beaulieu (1985) point to similar glacier extent during LIA on the nearby Marinét glacier (1.5 km further ENE) supported by palynological dating.

Giving this probable past glaciological context and the permafrost conditions in the valley (Figure S1; Marcer et al., 2017), the Chauvet system likely progressively changed from an active system facing a retreating dynamics to a stagnant state, as encountered in similar situations (Capt et al., 2016; Hambrey et al., 2008; Bosson et al., 2015). Field evidence, measured pluri-decadal surface changes and geo-electrical interpretations strongly suggest the presence of massive dead ice of glacial origin in sectors C and D of the Chauvet system but disconnected from the present glacier dynamics. By contrast, sectors A and B may rather be composed of frozen sediments. Thus, a multi-phased origin and a multilayered ice-debris complex must be considered (e.g., Matthews et al., 2014). Observations of surface velocity display on the one hand, back creeping movements following the LIA glacier retreat for sectors A and B. On the other hand, the movements

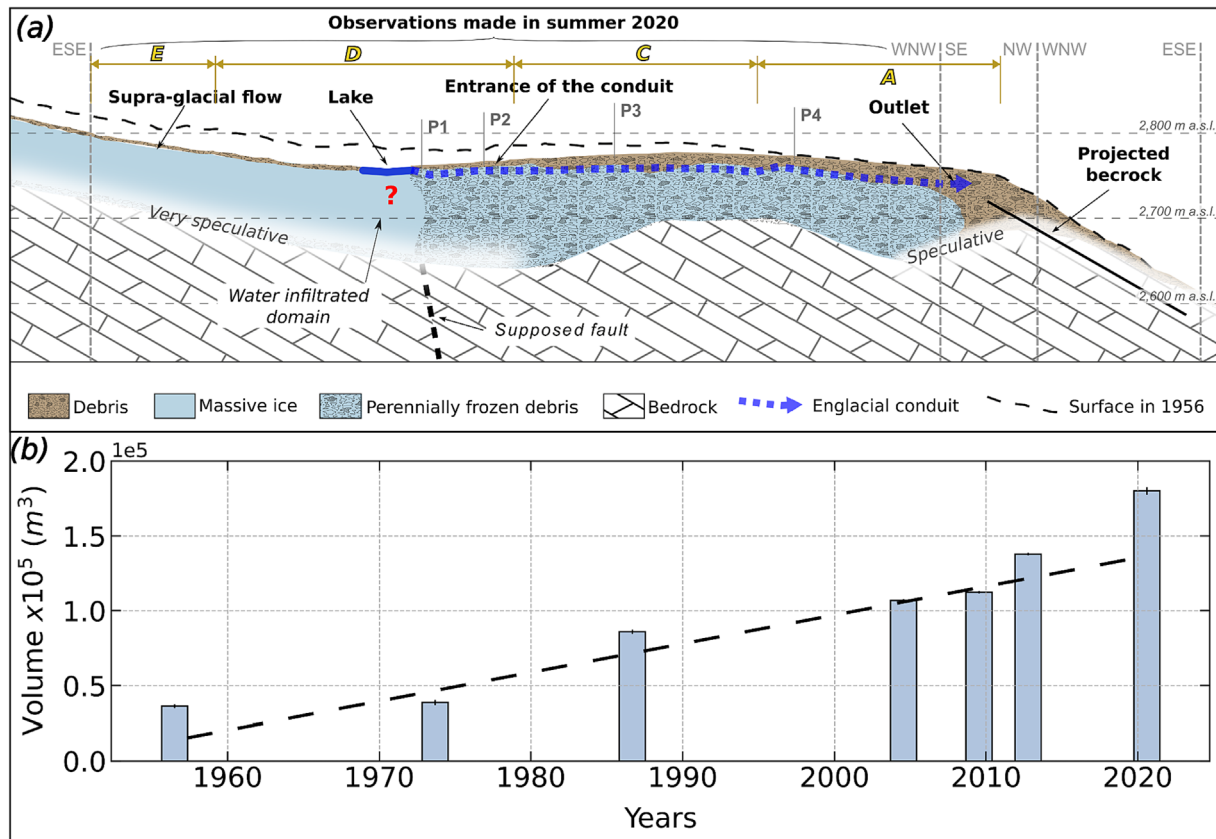


FIGURE 9 (a) Interpretation of longitudinal ERT profile over the talweg (red line on Figure 4) showing its extent in 1956 and 2020 (dashed and solid black lines, respectively) as well as the entrance and outlet zone of the conduit and possible route until bedrock outcrop (2750 m a.s.l.). Vertical grey dashed lines show change of direction of P5 longitudinal profile, and yellow letters correspond to geomorphological sectors on Figure 7. Bedrock topography between P3 and P4 is inferred from bedrock bulge on the right valley side and P5 ERT profile. (b) Changes in potential capacity of the Chauvet main thermokarst depression. Estimated using photogrammetric DSMs (Table 2) [Color figure can be viewed at wileyonlinelibrary.com]

of sector C are rather due to the flow of massive ice (Figure 6). This contrasted pattern in velocity is partially explained by the growth of the thermokarst area (sector D), likely related to the bucket shape of the bedrock (Kirkbride & Winkler, 2012), which has become progressively larger since 1970 due to the thermokarst lake and the enhanced ice melt ($-1.1 \pm 0.2 \text{ m a}^{-1}$, Figure 5). This topographic depression could have led to flow concentration of sector B oriented towards its centre as well as the movements towards the talweg (Figure 8). The observed acceleration after the 2000s could be likely explained by the mechanical disruption (i.e., rearrangement material) as well as permafrost degradation (Cusicanqui et al., 2021; Gärtner-Roer et al., 2022) and water availability within the landforms (Cicoira et al., 2019). Finally, the concave configuration of the Chauvet system (Figure 4) is favourable for the formation of the supraglacial lake by constantly feeding it with water originating from snow and ice melt and filling a natural depression, which experiences thermokarst conditions (Harris et al., 2001; Lin et al., 2016).

5.2 | Lake drainage and outburst floods

5.2.1 | Origins of conduit

When thermokarst lakes reach their maximum level, an 'overflow channel' is often visible at the surface (Gärtner-Roer et al., 2022;

Kääb & Haeberli, 2001). Enhanced water runoff promotes the formation of conduits due to sub- or intra-glacial water discharge (Haeberli, 2013). This surface channel is formed by the mechanical erosion caused by the flow of water in the ice. In the Chauvet system, the well-developed conduit (Figures 2b and S3) seems to be the consequence of an initial supra-glacial stream that evolves later in a near-surface channel continually incised vertically/laterally towards the bedrock. Once the conduit is sufficiently formed, it can be enclosed and become a subsurface conduit in the second stage, as encountered in similar situations (Fountain & Walder, 1998; Gulley et al., 2009). This hypothesis is supported by the location of the talweg (already visible on the oldest 1948 aerial photograph) as well as the continuous surface lowering of the talweg, due to ice-melt (Figure 8).

The current existence of the conduit can be still supported by the underground/englacial water circulation (upstream and downstream from sector D) and the anomalies encountered on the P2 ERT profile, which may indicate an empty/water-filled cavity (at a depth of 3–5 m; Figure 4) likely corresponding to the entrance of the conduit (3–4 m in diameter). The conduit seems to be connected to the thermokarst lake, with a mobile entry observed only on a couple of occasions (Figures 2c, S3 and S4), whereas the outlet of the conduit appears to remain relatively stable (Figure S9). The location and the geometry of the conduit were not visible on the other ERT profiles, probably due to the limited resolution of ERT surveys and to the size of the conduit, which is likely smaller down valley.

Regarding the internal development of the conduit, recent studies highlight the role of the bedrock topography on the development and sinuosity of an englacial conduit (Egli et al., 2021). At the Chauvet site, it could be also conditioned by the strong contrast of the terrain shown by the very different resistivities observed on the left and right hand side of the valley. An implication of this could be the difference in ice content of frozen materials (e.g., Hauck & Kneisel, 2008; Kunz & Kneisel, 2020; Scapozza, 2013), as well as different thermal regimes, as encountered in debris-covered glaciers (Hodgkins, 1997; Stuart et al., 2003). Nevertheless, as no internal temperature is available to support this hypothesis, caution is called for this interpretation.

5.2.2 | Mechanism controlling the conduit development

Once the conduit is developed, two main mechanisms control its dynamics: opening and closure. Regarding the conduit opening, it mainly results from frictional heat dissipated from the running water that melts the tunnel walls (Clarke, 2003; Spring & Hutter, 1981), while the sinuosity depends on the thickness of the debris layer and on the debris-size (Boyd et al., 2004). Therefore, enlargement of the conduit depends on both water discharge and water temperature, which will determine the opening rate (Röthlisberger, 1972). According to Vincent, Auclair, et al. (2010), slight variations in water temperature (0.8°C in the case of Rochemelon Glacier, French Alps) could modulate the erosion rate of the ice in the outlet channel of a supraglacial lake.

According to annual RTM reports and the present study, since 2002, a permanent thermokarst lake of varying size (never bigger than 2000 m²) forms every year accompanied by an ice cliff visible towards the surface (RTM, 2021, personal communication, April 23, 2021). The fact that water could be heard flowing underneath the debris layer and could be seen at the outlet (Figure S9) during the 2020 field campaign suggests that the conduit is always open (at least partially) outside outburst periods; thus, water can be evacuated efficiently. However, in the years outburst floods occurred, an unusually big lake was observed (area 18 times bigger than average, see Table S4 and Figure 9 and S5) suggesting the conduit was closed/obstructed. According to the S2M/SAFRAN dataset, no clear relation between the outburst events and exceptional rainfall or high snow/ice melt rates could be made.

Regarding the closure of the conduit, it can be caused by two processes: (a) the creep of ice at depth, where the closure rate is faster in larger channels than in smaller ones but is less sensitive to size than the opening rate, and (b) enclosure by obstruction due to collapse (Gulley et al., 2009). In the Chauvet system, it may be one consequence of the creep process cumulated for several years. This hypothesis is supported by the converging creep flows towards the talweg observed on sectors A and C (Figure 6). Close to sector D, sector B moves two times faster than sector C (Figure 6b). Further down, between the P3 and P4 ERT profiles, surface velocities are less pronounced, and sector A moves twice slower than the sector C area, likely caused by the enhanced creep due to the presence of massive ice. Some local collapses could also be part of the conduit closure (Figures S3–S5).

5.2.3 | Role of geology

Lastly, the geological context of the Chauvet system and the possibility of water drainage through a karstic network and the influence of permafrost conditions within the karstic network may also play a role. Glacio-karst environments are poorly known due to the complexity and huge effort required for their study (Veress, 2019). In the Chauvet watershed, evidence of karstification (e.g., lapiez and cave entrance) can be found in the landscape (Ford, 1983; Maire, 1978; Nicod, 1984). The presence of three transverse geological faults, the first located below the thermokarst system and the other two located down valley from the frontal slope at 2500 and 2300 m a.s.l., respectively, water was observed on these two faults on some occasions (Figure S16). The presence of a karstic water network cannot be excluded, although no evidence of vertical drainage of the thermokarst can be observed.

5.3 | Possible future development of the lake

The likelihood of an outburst flood depends on many different factors including potential flood volume, outburst mechanisms, erosion and deposition processes, and distance to infrastructures (Allen et al., 2022). Although it is beyond the scope of this study to analyse all these aspects of the risk relative to a potential outburst flood in the Chauvet system, we can nevertheless provide some information concerning potential future events.

In the historical context of the Chauvet system and given our analysis of current conditions, our results strongly suggest that another outburst flood could occur in the future. First, in the current glaciological context, 60% of the surface area (notably sectors E, D and C) contain an important proportion of massive ice below the debris layer (40 ± 10 m thick on average, Figure 4). Further, the predominant 'bucket shape' topography and continuously growing water storage capacity, which has increased by a factor of 5 since 1948 (Figure 9) allows potential storage of 180 000 ± 450 m³ of water. Moreover, the current slope between the lake and the outlet sector is 10° (20 m in elevation), that is, sufficient for drainage to occur.

6 | CONCLUSIONS

An interdisciplinary study of glacial and periglacial materials and landforms was performed over the Chauvet system. This multidisciplinary analysis opens new insights into the complex interaction between glacial and permafrost processes, as well as the related dynamics of complex ice-related landforms. The photogrammetric reconstruction over seven decades and geomorphological mapping shows a heterogeneous response to current climate forcing. Indeed, high thinning rates and highest surface velocities correspond to the massive-ice materials (e.g., dead-ice body covered by debris), in accordance with other debris-covered glaciers. On the other hand, more limited and contrasted patterns have been found in periglacial features (e.g., rock glacier) as observed in other study sites in the European Alps.

The presence of massive ice-melt (i.e., thermokarst lake) and the effects of topographic conditions (i.e., bucket shape of the thermokarst zone) have favoured the evolution of the associated

topographic depression and led to a progressive increase in size of the thermokarst lake since 1948. Currently, the topographic depression has a water storage capacity of $180\,000 \pm 450\,000\text{ m}^3$ (twice the volume of the 2008 maximum event).

The measurements documented through the geophysical soundings show a strong contrast between left-hand side ($1 \times 10^7\text{ Ohm m}$) and right-hand side ($1 \times 10^5\text{ Ohm m}$) as well as the upper and lower sector. This contrast is mainly related to the nature of sub-surface materials and the local permafrost conditions and could likely favour water circulation within the subsurface ice and thus, the development of the sub-surface conduit.

The GLOF events seem to be a consequence of closure and opening of the conduit triggered by the creep of frozen materials cumulated over several years (gravitational re-adjustment of frozen materials and flow of buried ice) which prevents the system from efficiently evacuating the surface water. It therefore results from complex and functional interactions between glacial and periglacial features, that is, the massive dead-ice body covered with debris, the frozen debris and the rock glacier, with contrasted dynamics notably on surface velocity and thickness changes.

Although the exact mechanism leading to the outburst floods remains still poorly understood, this study can serve as a base for future studies because it provides important insights into the complex dynamics of the interplayed materials, which need to be studied in more detail. Further studies (i.e., numerical simulations) as well as more observational data are needed to better understand the processes occurring at the site. Additional measurements (e.g., ice thickness distribution, ground/ice temperatures, lake water levels and temperature) are also required to better assess the origins of outburst floods. In this context, 4D (time-lapse) tomography of the conductivity and chargeability to be used to get more insight into the dynamics of this process that could be imaged over time.

AUTHOR CONTRIBUTIONS

Conceptualization: Diego Cusicanqui, Antoine Rabatel and Xavier Bodin. **Funding acquisition:** Antoine Rabatel and Xavier Bodin. **Methodology:** Diego Cusicanqui, Xavier Bodin, Pierre-Allain Duvillard and Philippe Schoeneich. **Investigation:** Diego Cusicanqui, Xavier Bodin, Antoine Rabatel, Pierre-Allain Duvillard, Philippe Schoeneich and Johan Berthet. **Resources:** Diego Cusicanqui, Alain Assier, Peyron Michel and Stéphane Roudnitska. **Supervision:** Diego Cusicanqui, Antoine Rabatel, Xavier Bodin, André Revil and Philippe Schoeneich. **Writing—initial draft:** Diego Cusicanqui, Antoine Rabatel, Xavier Bodin, Pierre-Allain Duvillard and Philippe Schoeneich. **Writing—reviewing and editing:** Diego Cusicanqui, Antoine Rabatel, Xavier Bodin, André Revil and Philippe Schoeneich.

ACKNOWLEDGEMENTS

This work was supported by the French National Research Agency in the framework of the *Investissements d'Avenir* programmes: Risk@UGA (ANR-15-IDEX-02) and LabEx OSUG@2020 (ANR10 LABX56). The Pléiades images were kindly provided by the *Dispositif Institutionnel National d'Approvisionnement Mutualisé en Imagerie Satellitaire*, DINAMIS, through Pleiades project 'Emerging risks related to the dark side of the Alpine cryosphere' (©CNES/Airbus). This study is also part of the PERMARISK project funded by the European Regional Development Fund (grant POIA PA0004100).

We thank Météo-France and the USMB library for meteorological data. We are grateful to Raphaëlle Charvet and Hugo Collomb from RTM; François-Luc Cimelière, Clément Cassoti and Simon Alessina from EDyTEM; Alexandre Baratier from STYX4D; and Annabelle Matuszak and Raphael Loiseau from IUGA for their precious help during field surveys. Thanks also to Ugo Nanni, Benjamin Lehmann and Christian Vincent for fruitful discussions on the topics of the present paper and to Daphne Goodfellow for reviewing the English. Finally, we thank to Wilfried Haerberli and two anonymous reviewers whose comments and suggestions greatly helped to improve and clarify this manuscript.

DATA AVAILABILITY STATEMENT

Main data supporting the findings of this study could be accessed through the Zenodo data repository (<https://zenodo.org/deposit/7554198>). Data include raw DEM's and surface velocities computed for different periods. Videos 1–3 were acquired from different points over the Chauvet glacial and periglacial system during the outburst flood that occurred on 17 July 2008. Video 4 (shot by M. Peyron, RTM) is a view of an outburst flood event at the confluence with the Ubaye river (1690 m a.s.l.). Additional information is available from Diego Cusicanqui (diego.cusicanqui.vg@gmail.com) or Xavier Bodin (xavier.bodin@univ-smb.fr) upon request.

ORCID

Diego Cusicanqui  <https://orcid.org/0000-0002-4681-1111>

REFERENCES

- Abdulsamad, F., Revil, A., Ghorbani, A., Toy, V., Kirilova, M., Coperey, A., et al. (2019) Complex conductivity of graphitic schists and sandstones. *Journal of Geophysical Research: Solid Earth*, 124(8), 8223–8249. Available from: <https://doi.org/10.1029/2019JB017628>
- Allen, S., Frey, H., Haerberli, W., Huggel, C., Chiarle, M. & Geertsema, M. (2022) Assessment principles for glacier and permafrost hazards in mountain regions. *Oxford Research Encyclopedia of Natural Hazard Science*, 28. Available from: <https://doi.org/10.1093/acrefore/9780199389407.013.356>
- Assier, A. & Evin, M. (1995). Cryokarst et vidanges glaciaires au glacier de Chauvet (Huata-Ubaye, Alpes Françaises du Sud). Actes du 3ème symposium international Cavités glaciers et cryokarst en régions polaires et de haute montagne 34: 83–87.
- Assier, A. (2018) *Glaciers et Glaciers rocheux*. Sabença de la Valèia, Barcelonnette, France: Vallée de l'Ubaye ISBN: 978-2908-103-717.
- Assier, A., Fabre, D., Evin, M. (1994). Structure interne du cryokarst et vidanges du glacier de Chauvet (Haute-Ubaye). Presented at the "Société Hydrotechnique de France (SHF conference)", Section Glaciologie. Grenoble, 10–11 mars France.
- Besl, P.J. & McKay, N.D. 1992. Method for registration of 3-D shapes. Proc. SPIE 1611, Sensor Fusion IV: Control Paradigms and Data Structures. 586–606 <https://doi.org/10.1117/12.57955>
- Boeckli, L., Brenning, A., Gruber, S. & Noetzli, J. (2012) Permafrost distribution in the European Alps: calculation and evaluation of an index map and summary statistics. *The Cryosphere*, 6(4), 807–820. Available from: <https://doi.org/10.5194/tc-6-807-2012>
- Bosson, J.-B. & Lambiel, C. (2016) Internal structure and current evolution of very small debris-covered glacier systems located in Alpine permafrost environments. *Frontiers in Earth Science*, 4, 39. Available from: <https://doi.org/10.3389/feart.2016.00039>
- Bosson, J.-B., Deline, P., Bodin, X., Schoeneich, P., Baron, L., Gardent, M., et al. (2015) The influence of ground ice distribution on geomorphic dynamics since the Little Ice Age in proglacial areas of two cirque glacier systems. *Earth Surface Processes and Landforms*, 40(5), 666–680. Available from: <https://doi.org/10.1002/esp.3666>

- Boyd, B., Goetz, S.L. & Ham, N.R. (2004) Supraglacial stream incision into debris-covered ice, Matanuska Glacier, AK. *Geological Society of America Abstracts with Programs*, 36, 11.
- Buckel, C. (2010) *Etude de la stabilité du glacier rocheux du fond de Chauvet. Internship*. Strasbourg, France: Université de Strasbourg: École et Observatoire des Sciences de la Terre (EOST).
- Capt, M., Bosson, J.-B., Fischer, M., Micheletti, N. & Lambiel, C. (2016) Decadal evolution of a very small heavily debris-covered glacier in an Alpine permafrost environment. *Journal of Glaciology*, 62(233), 535–551. Available from: <https://doi.org/10.1017/jog.2016.56>
- Cicoira, A., Beutel, J., Faillettaz, J. & Vieli, A. (2019). Water controls the seasonal rhythm of rock glacier flow. *Earth and Planetary Science Letters*, 528, 115844. Available from: <https://doi.org/10.1016/j.epsl.2019.115844>
- Clague, J.J. & Evans, S.G. (2000) A review of catastrophic drainage of moraine-dammed lakes in British Columbia. *Quaternary Science Reviews*, 19(17–18), 1763–1783. Available from: [https://doi.org/10.1016/S0277-3791\(00\)00090-1](https://doi.org/10.1016/S0277-3791(00)00090-1)
- Clarke, G.K.C. (2003) Hydraulics of subglacial outburst floods: new insights from the Spring–Hutter formulation. *Journal of Glaciology*, 49(165), 299–313. Available from: <https://doi.org/10.3189/172756503781830728>
- Conrad, O., Bechtel, B., Bock, M., Dietrich, H., Fischer, E., Gerlitz, L., et al. (2015) System for Automated Geoscientific Analyses (SAGA) v. 2.1.4. *Geoscientific Model Development Discussions*, 8, 2271–2312. Available from: <https://doi.org/10.5194/gmdd-8-2271-2015>
- Coperey, A., Revil, A., Abdulsamad, F., Stutz, B., Duvillard, P.A. & Ravel, L. (2019) Low-frequency induced polarization of porous media undergoing freezing: preliminary observations and modeling. *Journal of Geophysical Research: Solid Earth*, 124(5), 4523–4544. Available from: <https://doi.org/10.1029/2018JB017015>
- Cusicanqui, D., Rabatel, A., Vincent, C., Bodin, X., Thibert, E. & Francou, B. (2021) Interpretation of volume and flux changes of the Laurichard Rock Glacier between 1952 and 2019, French Alps. *Journal of Geophysical Research: Earth Surface*, 126(9), e2021JF006161. Available from: <https://doi.org/10.1029/2021JF006161>
- Dahlin, T. & Zhou, B. (2004) A numerical comparison of 2D resistivity imaging with 10 electrode arrays. *Geophysical Prospecting*, 52(5), 379–398. Available from: <https://doi.org/10.1111/j.1365-2478.2004.00423.x>
- Duvillard, P.A., Revil, A., Qi, Y., Ahmed, A.S., Coperey, A. & Ravel, L. (2018) Three-dimensional electrical conductivity and induced polarization tomography of a rock glacier. *Journal of Geophysical Research: Solid Earth*, 123(11), 9528–9554. Available from: <https://doi.org/10.1029/2018JB015965>
- Duvillard, P.-A., Magnin, F., Revil, A., Legay, A., Ravel, L., Abdulsamad, F., et al. (2021) Temperature distribution in a permafrost-affected rock ridge from conductivity and induced polarization tomography. *Geophysical Journal International*, 225(2), 1207–1221. Available from: <https://doi.org/10.1093/gji/ggaa597>
- Egli, P.E., Irving, J. & Lane, S.N. (2021) Characterization of subglacial marginal channels using 3-D analysis of high-density ground-penetrating radar data. *Journal of Glaciology*, 67(264), 759–772. Available from: <https://doi.org/10.1017/jog.2021.26>
- Emmer, A., Harrison, S., Mergili, M., Allen, S., Frey, H. & Huggel, C. (2020) 70 years of lake evolution and glacial lake outburst floods in the Cordillera Blanca (Peru) and implications for the future. *Geomorphology*, 365, 107178. Available from: <https://doi.org/10.1016/j.geomorph.2020.107178>
- Etzelmüller, B., Guglielmin, M., Hauck, C., Hilbich, C., Hoelzle, M., Isaksen, K., et al. (2020) Twenty years of European mountain permafrost dynamics—the PACE legacy. *Environmental Research Letters*, 15(10), 1040–1070. Available from: <https://doi.org/10.1088/1748-9326/abae9d>
- Evin, M. & de Beaulieu, J.L. (1985) Nouvelles données sur l'âge de la mise en place et les phases d'activité du glacier rocheux de Marinnet I (Haute-Ubaye, Alpes du Sud françaises). *Méditerranée*, 56(4), 21–30. Available from: <https://doi.org/10.3406/medit.1985.2330>
- Ford, D.C. (1983) The physiography of the Castleguard Karst and Columbia icefields area, Alberta, Canada. *Arctic and Alpine Research*, 15(4), 427–436. Available from: <https://doi.org/10.2307/1551230>
- Fountain, A.G. & Walder, J.S. (1998) Water flow through temperate glaciers. *Reviews of Geophysics*, 36(3), 299–328. Available from: <https://doi.org/10.1029/97RG03579>
- Gardent, M. 2014. Inventaire et retrait des glaciers dans les Alpes françaises depuis la fin du Petit Age Glaciaire, PhD Thesis. (Université Grenoble Alpes). 455. (NNT: 2014GRENA008). (tel-01062226)
- Gidon, M. (1994) Notice explicative, Carte géol. In: *France (1/50000), feuille Aiguille de Chambeyron (872)*. Orléans: BRGM.
- Gidon, M., Kerckhove, C., Michard, A., Tricart, P., Gotteland, P., Gout, C., et al. (1994). Carte géol. France (1/50000), feuille Aiguille de Chambeyron (872).
- Guibert, L. (2013) *Runout modelling of debris flows released from rock glaciers. Internship*. Strasbourg, France: Université de Strasbourg: École et Observatoire des Sciences de la Terre (EOST).
- Gulley, J.D., Benn, D.I., Müller, D. & Luckman, A. (2009) A cut-and-closure origin for englacial conduits in uncrevassed regions of polythermal glaciers. *Journal of Glaciology*, 55(189), 66–80. Available from: <https://doi.org/10.3189/002214309788608930>
- Gärtner-Roer, I., Brunner, N., Delaloye, R., Haerberli, W., Käb, A. & Thee, P. (2022) Glacier-permafrost relations in a high-mountain environment: 5 decades of kinematic monitoring at the Gruben site, Swiss Alps. *The Cryosphere*, 16(5), 2083–2101. Available from: <https://doi.org/10.5194/tc-16-2083-2022>
- Haerberli, W. (2005) Investigating glacier-permafrost relationships in high-mountain areas: historical background, selected examples and research needs. *Geological Society, London, Special Publications*, 242(1), 29–37. Available from: <https://doi.org/10.1144/GSL.SP.2005.242.01.03>
- Haerberli, W. (2013) Mountain permafrost—research frontiers and a special long-term challenge. *Cold Regions Science and Technology*, 96, 71–76. Available from: <https://doi.org/10.1016/j.coldregions.2013.02.004>
- Haerberli, W., Käb, A., Mühl, D.V. & Teyssie, P. (2001) Prevention of outburst floods from periglacial lakes at Grubengletscher, Valais, Swiss Alps. *Journal of Glaciology*, 47(156), 111–122. Available from: <https://doi.org/10.3189/172756501781832575>
- Hambrey, M.J., Quincey, D.J., Glasser, N.F., Reynolds, J.M., Richardson, S.J. & Clemmens, S. (2008) Sedimentological, geomorphological and dynamic context of debris-mantled glaciers, Mount Everest (Sagarmatha) region, Nepal. *Quaternary Science Reviews*, 27(25–26), 2361–2389. Available from: <https://doi.org/10.1016/j.quascirev.2008.08.010>
- Harris, C., Davies, M.C.R. & Etzelmüller, B. (2001) The assessment of potential geotechnical hazards associated with mountain permafrost in a warming global climate. *Permafrost and Periglacial Processes*, 12(1), 145–156. Available from: <https://doi.org/10.1002/ppp.376>
- Harris, S., Brouchkov, A. & Guodong, C. (2018) *Geocryology. Characteristics and use of frozen ground and permafrost landforms*, 1st edition. London, UK: CRC Press.
- Hauck, C. & Kneisel, C. (2008) *Applied geophysics in periglacial environments*. Cambridge: Cambridge University Press.
- Hock, R., Rasul, G., Adler, C., Cáceres, B., Gruber, S., Hirabayashi, Y., et al. (2019) High mountain areas. In: Pörtner, H.-O., Roberts, D.C., Masson-Delmotte, V., Zhai, P., Tignor, M., Poloczanska, E., et al. (Eds.) *IPCC special report on the ocean and cryosphere in a changing climate*. Cambridge, UK and New York, NY, USA: Cambridge University Press, pp. 131–202 <https://doi.org/10.1017/9781009157964.004>
- Hodgkins, R. (1997) Glacier hydrology in Svalbard, Norwegian high arctic. *Quaternary Science Reviews*, 16(9), 957–973. Available from: [https://doi.org/10.1016/S0277-3791\(97\)00032-2](https://doi.org/10.1016/S0277-3791(97)00032-2)
- Hugonnet, R., McNabb, R., Berthier, E., Menounos, B., Nuth, C., Girod, L., et al. (2021) Accelerated global glacier mass loss in the early twenty-first century. *Nature*, 592(7856), 726–731. Available from: <https://doi.org/10.1038/s41586-021-03436-z>
- IGN. (2021). “Cartes d'état majeur” accessible depuis Remonter le temps [online]. Available from: [//remonterletemps.ign.fr](https://remonterletemps.ign.fr) (Accessed 10 April 2021)

- Kemna, A., Binley, A., Cassiani, G., Niederleithinger, E., Revil, A., Slater, L., et al. (2012) An overview of the spectral induced polarization method for near-surface applications. *Near Surface Geophysics*, 10(6), 453–468. Available from: <https://doi.org/10.3997/1873-0604.2012027>
- Kirkbride, M. & Winkler, S. (2012) Correlation of Late Quaternary moraines: impact of climate variability, glacier response, and chronological resolution. *Quaternary Science Reviews*, 46, 1–29. Available from: <https://doi.org/10.1016/j.quascirev.2012.04.002>
- Kirschbaum, D., Watson, C.S., Rounce, D.R., Shugar, D.H., Kargel, J.S., Haritashya, U.K., et al. (2019) The state of remote sensing capabilities of cascading hazards over High Mountain Asia. *Frontiers in Earth Science*, 7, 197. Available from: <https://doi.org/10.3389/feart.2019.00197>
- Kneisel, C. (2006) Assessment of subsurface lithology in mountain environments using 2D resistivity imaging. *Geomorphology*, 80(1–2), 32–44. Available from: <https://doi.org/10.1016/j.geomorph.2005.09.012>
- Kunz, J. & Kneisel, C. (2020) Glacier–permafrost interaction at a thrust moraine complex in the glacier Forefield Muragl, Swiss Alps. *Geosciences*, 10, 205. Available from: <https://doi.org/10.3390/geosciences10060205>
- Kääb, A. & Haeblerli, W. (2001) Evolution of a High-Mountain Thermokarst Lake in the Swiss Alps. *Arctic, Antarctic, and Alpine Research*, 33(4), 385–390. Available from: <https://doi.org/10.2307/1552546>
- Kääb, A., Huggel, C., Fischer, L., Guex, S., Paul, F., Roer, I., et al. (2005) Remote sensing of glacier- and permafrost-related hazards in high mountains: an overview. *Natural Hazards and Earth System Sciences*, 5(4), 527–554. Available from: <https://doi.org/10.5194/nhess-5-527-2005>
- Lambiel, C., Maillard, B., Kummert, M. & Reynard, E. (2016) Geomorphology of the Hérens valley (Swiss Alps). *Journal of Maps*, 12(1), 160–172. Available from: <https://doi.org/10.1080/17445647.2014.999135>
- Lin, Z., Luo, J. & Niu, F. (2016) Development of a thermokarst lake and its thermal effects on permafrost over nearly 10 yr in the Beiluhe Basin, Qinghai-Tibet Plateau. *Geosphere*, 12(2), 632–643. Available from: <https://doi.org/10.1130/GES01194.1>
- Loke, M.H. & Barker, R.D. (1996) Rapid least-squares inversion of apparent resistivity pseudosections by a quasi-Newton method. *Geophysical Prospecting*, 44(1), 131–152. Available from: <https://doi.org/10.1111/j.1365-2478.1996.tb00142.x>
- Maire, R. (1978) Les karsts sous-glaciaires et leurs relations avec le karst profond. *Revue de Géographie Alpine*, 66(2), 139–148. Available from: <https://doi.org/10.3406/rga.1978.2118>
- Marcet, M., Bodin, X., Brenning, A., Schoeneich, P., Charvet, R. & Gottardi, F. (2017) Permafrost favorability index: spatial modeling in the French Alps using a rock glacier inventory. *Frontiers in Earth Science*, 5, 105. Available from: <https://doi.org/10.3389/feart.2017.00105>
- Marcet, M., Cicoira, A., Cusicanqui, D., Bodin, X., Echelard, T., Obregon, R., et al. (2021) Rock glaciers throughout the French Alps accelerated and destabilised since 1990 as air temperatures increased. *Nature Communications Earth & Environment*, 2(1), 1, 81–11. Available from: <https://doi.org/10.1038/s43247-021-00150-6>
- Matthews, J.A., Winkler, S. & Wilson, P. (2014) Age and origin of ice-cored moraines in Jotunheimen and Breheimen, southern Norway: insights from Schmidt-hammer exposure-age dating. *Geografiska Annaler: Series A, Physical Geography*, 96(4), 531–548. Available from: <https://doi.org/10.1111/geoa.12046>
- Maurer, H. & Hauck, C. (2007) Geophysical imaging of alpine rock glaciers. *Journal of Glaciology*, 53(180), 110–120. Available from: <https://doi.org/10.3189/172756507781833893>
- Mergili, M., Jaboyedoff, M., Pullarello, J. & Pudasaini, S.P. (2020) Back calculation of the 2017 Piz Cengalo–Bondo landslide cascade with r. avaflow: what we can do and what we can learn. *Natural Hazards and Earth System Sciences*, 20, 505–520. Available from: <https://doi.org/10.5194/nhess-20-505-2020>
- Mertes, J.R., Gulley, J.D., Benn, D.I., Thompson, S.S. & Nicholson, L.I. (2017) Using structure-from-motion to create glacier DEMs and orthoimagery from historical terrestrial and oblique aerial imagery: SfM on differing historical glacier imagery sets. *Earth Surface Processes and Landforms*, 42(14), 2350–2364. Available from: <https://doi.org/10.1002/esp.4188>
- Mollaret, C., Hilbich, C., Pellet, C., Flores-Orozco, A., Delaloye, R. & Hauck, C. (2019) Mountain permafrost degradation documented through a network of permanent electrical resistivity tomography sites. *The Cryosphere*, 13(10), 2557–2578. Available from: <https://doi.org/10.5194/tc-13-2557-2019>
- Nicod, J. (1984) Les massifs karstiques des Alpes occidentales: trame structurale et bioclimatique. Présentation de la carte d'ensemble au 1/750 000. *Karstologia*, 3(1), 3–11. Available from: <https://doi.org/10.3406/karst.1984.2062>
- Ragetti, S., Bolch, T. & Pellicciotti, F. (2016) Heterogeneous glacier thinning patterns over the last 40 years in Langtang Himal, Nepal. *The Cryosphere*, 10(5), 2075–2097. Available from: <https://doi.org/10.5194/tc-10-2075-2016>
- Ravel, L. & Deline, P. (2015) Rockfall hazard in the Mont Blanc Massif increased by the current atmospheric warming. In: Lollino, G., Manconi, A., Clague, J., Shan, W. & Chiarle, M. (Eds.) *Engineering geology for society and territory—volume 1*. Cham: Springer International Publishing, pp. 425–428. https://doi.org/10.1007/978-3-319-09300-0_81
- Revil, A., Johnson, T.C. & Finizola, A. (2010) Three-dimensional resistivity tomography of Vulcan's forge, Vulcano Island, southern Italy. *Geophysical Research Letters*, 37(15), 308. Available from: <https://doi.org/10.1029/2010GL043983>
- Revil, A., Soueid Ahmed, A., Coperey, A., Ravel, L., Sharma, R. & Panwar, N. (2020) Induced polarization as a tool to characterize shallow landslides. *Journal of Hydrology*, 589, 125369. Available from: <https://doi.org/10.1016/j.jhydrol.2020.125369>
- Rodríguez, A., Mas, S., Richard, D. & Chirié, F. (2008). IGN Spain and IGN France collaboration to set up cross border INSPIRE compliant services. 10.
- Röthlisberger, H. (1972) Water pressure in intra- and subglacial channels*. *Journal of Glaciology*, 11(62), 177–203. Available from: <https://doi.org/10.3189/S0022143000022188>
- Scambos, T.A., Dutkiewicz, M.J., Wilson, J.C. & Bindschadler, R.A. (1992) Application of image cross-correlation to the measurement of glacier velocity using satellite image data. *Remote Sensing of Environment*, 42(3), 177–186. Available from: [https://doi.org/10.1016/0034-4257\(92\)90101-0](https://doi.org/10.1016/0034-4257(92)90101-0)
- Scapozza, C. (2013) *Stratigraphie, morphodynamique, paléoenvironnements des terrains sédimentaires meubles à forte déclivité du domaine périglaciaire alpin*. *Géovisions*, Vol. 40. Lausanne, Switzerland: Université de Lausanne, Institut de géographie et durabilité, p. 551. PhD diss.
- Schoeneich, P. (1993) *Comparaison des systèmes de légende français, allemand et suisse - principes de la légende IGUL*. In Schoeneich P and Reynard E.(eds), *Cartographie géomorphologique - Cartographie des Risques*. Lausanne, Switzerland: Institut de Géographie Université de Lausanne, Travaux & Recherches No. 9: 15–24.
- Shean, D.E., Alexandrov, O., Moratto, Z.M., Smith, B.E., Joughin, I.R., Porter, C., et al. (2016) An automated, open-source pipeline for mass production of digital elevation models (DEMs) from very-high-resolution commercial stereo satellite imagery. *ISPRS Journal of Photogrammetry and Remote Sensing*, 116, 101–117. Available from: <https://doi.org/10.1016/j.isprsjprs.2016.03.012>
- Smith, M.J. (2011) Chapter eight—digital mapping: visualisation, interpretation and quantification of landforms. In: Smith, M.J., Paron, P. & Griffiths, J.S. (Eds.) *Developments in earth surface processes*. Oxford, UK: Elsevier, pp. 225–251. <https://doi.org/10.1016/B978-0-444-53446-0.00008-2>
- Spring, U. & Hutter, K. (1981) Numerical studies of Jökulhlaups. *Cold Regions Science and Technology*, 4(3), 227–244. Available from: [https://doi.org/10.1016/0165-232X\(81\)90006-9](https://doi.org/10.1016/0165-232X(81)90006-9)
- Stuart, G., Murray, T., Gamble, N., Hayes, K. & Hodson, A. (2003) Characterization of englacial channels by ground-penetrating radar: an example from austre Brøggerbreen, Svalbard. *Journal of Geophysical Research: Solid Earth*, 108(B11), 2525. Available from: <https://doi.org/10.1029/2003JB002435>

- Veress M. 2019. *Karst landforms of glaciokarst and their development*. In *Glaciokarsts*, Veress M, Telbisz T, Tóth G, Lóczy DA Ruban D, and M. Gutak (eds). Springer International Publishing: Cham; 115–219.
- Vernay, M., Lafaysse, M., Hagenmuller, P., Nheili, R., Verfaillie, D. & Morin, S. (2020). The S2M meteorological and snow cover reanalysis in the French mountainous areas (1958–present). [Data set] <https://doi.org/10.25326/37>
- Vincent, C., Auclair, S. & le Meur, E. (2010) Outburst flood hazard for glacier-dammed lac de Rochemelon, France. *Journal of Glaciology*, 56(195), 91–100. Available from: <https://doi.org/10.3189/002214310791190857>
- Vincent, C., Garambois, S., Thibert, E., Lefèbvre, E., le Meur, E. & Six, D. (2010) Origin of the outburst flood from Glacier de Tête Rousse in 1892 (Mont Blanc area, France). *Journal of Glaciology*, 56(198), 688–698. Available from: <https://doi.org/10.3189/002214310793146188>
- Westoby, M.J., Brasington, J., Glasser, N.F., Hambrey, M.J. & Reynolds, J.M. (2012) ‘Structure-from-motion’ photogrammetry: a low-cost, effective tool for geoscience applications. *Geomorphology*, 179, 300–314. Available from: <https://doi.org/10.1016/j.geomorph.2012.08.021>
- Wheaton, J.M., Brasington, J., Darby, S.E. & Sear, D.A. (2010) Accounting for uncertainty in DEMs from repeat topographic surveys: improved sediment budgets. *Earth Surface Processes and Landforms*, 35, 136–156. Available from: <https://doi.org/10.1002/esp.1886>

SUPPORTING INFORMATION

Additional supporting information can be found online in the Supporting Information section at the end of this article.

How to cite this article: Cusicanqui, D., Bodin, X., Duvillard, P.-A., Schoeneich, P., Revil, A., Assier, A. et al. (2023) Glacier, permafrost and thermokarst interactions in Alpine terrain: Insights from seven decades of reconstructed dynamics of the Chauvet glacial and periglacial system (Southern French Alps). *Earth Surface Processes and Landforms*, 48(13), 2595–2612. Available from: <https://doi.org/10.1002/esp.5650>